

# Transfer and reconstruction of the density matrix in off-axis electron holography

Falk Röder\*, Axel Lubk

Triebenberg Labor, Institut für Strukturphysik, Technische Universität Dresden, D-01062 Dresden, Germany



## ARTICLE INFO

### Article history:

Received 27 May 2014

Received in revised form

16 July 2014

Accepted 21 July 2014

Available online 31 July 2014

### Keywords:

Off-axis electron holography

Transmission cross-coefficient

Density matrix

## ABSTRACT

The reduced density matrix completely describes the quantum state of an electron scattered by an object in transmission electron microscopy. However, the detection process restricts access to the diagonal elements only. The off-diagonal elements, determining the coherence of the scattered electron, may be obtained from electron holography. In order to extract the influence of the object from the off-diagonals, however, a rigorous consideration of the electron microscope influences like aberrations of the objective lens and the Möllenstedt biprism in the presence of partial coherence is required. Here, we derive a holographic transfer theory based on the generalization of the transmission cross-coefficient including all known holographic phenomena. We furthermore apply a particular simplification of the theory to the experimental analysis of aloof beam electrons scattered by plane silicon surfaces.

© 2014 Elsevier B.V. All rights reserved.

## 1. Introduction

Intensity distributions recorded by transmission electron microscopy (TEM) generally depend on the probability density as well as the spatial and temporal coherence within the scattered electron beam after interaction with an object. For instance, high-resolution images obtained from elastically scattered electrons are modulated by the combined influence of coherent lens aberrations and the partially coherent source summarized in the transmission cross-coefficient (TCC) [1,2]. Even more importantly, different inelastic scattering processes [3–9] and statistical fluctuations within the object [10], within the energy and momentum distribution of the electron beam or within the surrounding environment [11–13] also change the coherence properties of the beam. These modulations can be effectively described within the framework of density matrix transfer through the object and electron microscope.

Regarding the transfer through the object, van Hove showed in 1954 that the dynamic form factor relates the diffracted intensity and density-density correlation in the object [14]. However, since this concept only describes the diagonal elements of the density matrix (intensities) detectable at the back focal plane, it is insufficient for considering image formation of inelastically scattered electrons at the image plane. Therefore, the dynamic form factor was later generalized to the mixed dynamic form factor (MDFF) [15] incorporating also the off-diagonals (i.e. coherence).

In first order Born approximation the MDFF is proportional to the cross-spectral density (known from classical optics) at the back focal plane [16]. The inverse temporal Fourier transformation of the cross-spectral density is called mutual coherence function in turn [17,18]. Equivalent to the cross-spectral density, the quantum mechanical density matrix description [19,20] was applied to describe inelastic scattering phenomena in first order and beyond [9]. The MDFF-concept provides powerful approximations describing image formation influenced by plasmon excitations [8,21–24], single electron excitations [25–30] and phonon excitations [25,26,24].

To obtain a comprehensive picture on the scattering process a measurement comprising both probability density and coherence is therefore indispensable. However, the quantum nature of the measurement process [31,32] prohibits direct access to this combined data in principle. This general information loss implies, e.g. the impossibility of exactly predicting the backward and forward evolution of intensity from a single intensity measurement (in the space below the object). This is the reason, why inelastic scattering cross-sections retrieved from measurements at the back focal plane of the objective lens have no or just very limited predictive power for the formation of intensities measured at the image plane.

Therefore we are interested in experimentally reconstructing the (reduced) density matrix of a probe electron after interaction with an object. Since information about the coherence is lost by intensity measurements, they have to be artificially encoded in the intensity distribution before measurement. This can be realized by relating different positions within the wave field with each other, i.e. by using electron holography [33,34]. In the off-axis type

\* Corresponding author.

E-mail address: [Falk.Roeder@Triebenberg.de](mailto:Falk.Roeder@Triebenberg.de) (F. Röder).

electron holography [35], the Möllenstedt biprism realizes a superposition of two partial waves in the image plane, which are separated by a certain distance in the object plane [36]. Thus, the resulting interference fringe pattern contains correlations of the wave field measurable in terms of local interference fringe contrast and phase shift with respect to a reference [37,35,38,39]. Especially, inelastically scattered electrons attenuate characteristically the fringe contrast, which was studied by means of inelastic electron holography in past [40–44]. Theoretical considerations [22,23] show that the coherence experimentally measured in this manner is related to distinguished off-diagonal elements of the electron beam density matrix selectable experimentally by changing the biprism voltage. Based on these results, we generally investigate the method off-axis electron holography for reconstructing the density matrix of inelastically scattered electrons. This requires a detailed transfer theory of the density matrix in a holographic TEM, which was partially considered already in Ref. [45]. For elastically scattered waves in conventional TEM, the transfer was described using the transmission cross-coefficient (TCC) [17, p. 530] applied to TEM imaging [1,2,46–50]. Similarly, the transfer of inelastically scattered electrons was described with the help of methods developed in classical optics [17, p. 537] using the propagation of mutual coherence [16,25,26,24]. But to our knowledge, only the *intensity* at the image or back focal plane was discussed. In this paper we develop in a first step a generalized transfer theory describing the *intensity and coherence* at various detection planes in the transmission electron microscope based on the concept of the TCC. In a second step, we incorporate the Möllenstedt biprism [36] and generally relate the recorded interference fringe pattern to the electron density matrix at the object exit plane. This is the prerequisite for the interpretation of further experimental results.

This paper is organized as follows. In Section 2, we formulate the transfer of the reduced density matrix of the probe electron  $\rho_s$  under partially coherent illumination. Here, we further generalize the TCC concept for the propagation of density matrices from the object to the image plane. This is the prerequisite for the discussion of the holographic transfer theory deduced in Section 3. There, we derive the holographic TCC describing in general the density matrix transfer in case of a general off-axis electron holographic experiment. We will interpret centre band and side-band contributions to the interference pattern in terms of modulated diagonal and off-diagonal elements of the density matrix at the object exit plane. We show that all phenomena in conventional off-axis electron holography are included in the presented theory. In Section 4, we introduce a procedure for density matrix reconstruction, which requires simplifications in the transfer theory. We deduce corresponding conditions and verify them numerically. In Section 5 we apply the developed procedure to a famous experiment as proposed in Ref. [51], which was intended to visualize the quantum-to-classical transition by decoherence: We reconstruct the density matrix from an interference fringe pattern of aloof beam electrons [52] inelastically scattered by a planar silicon surface.

## 2. Density matrix transfer in TEM

This section introduces the transfer of the density matrix using the concept of the TCC. We first relate the density matrix to the measurable current density. Subsequently we transfer the density matrix from the electron source plane downwards to the object plane, which is optically located in the far field of the electron source. Here, the electron beam is modulated by interaction with the object. Isoplanatic aberrations affecting the image plane are treated by density dependent phase shifts at the back focal plane of

the objective lens. By integration over the beam ensemble parameters we will identify the generalized TCC. Throughout this section we will employ twisted Seidel coordinates. That means we neglect image magnification and rotation in the following implying that coordinates at the image plane are the same as at the object plane for instance.

### 2.1. The density matrix of the probe electron

The time integrated current density (intensity) of the scattered electron beam is the main signal in transmission electron microscopy, which is detected, e.g. by CCD-cameras. The scattering of high energy electrons in the range of 20 keV–1 MeV leads to comparably small lateral momenta. Thus, the expectation value of the current density becomes proportional to the quantum mechanical probability density of the electron wave  $\psi_0$

$$\mathbf{j} = \frac{\hbar}{2im} (\psi_0^* \nabla \psi_0 - \psi_0 \nabla \psi_0^*) \approx \frac{\hbar \mathbf{k}_0}{m} |\psi_0|^2. \quad (1)$$

Here,  $m$  denotes the relativistic mass of the beam electron and  $\mathbf{k}_0$  is the initial mean wave vector. Due to interaction with the object the beam electron entangles with internal degrees of freedom of the object [31,32], i.e. the product of object ground state  $\tau_0(\xi)$  and the impinging beam electron  $\psi_0(\mathbf{r})$  transforms to

$$\Psi(\mathbf{r}, \xi) = \psi_0(\mathbf{r}) \tau_0(\xi) \rightarrow \sum_i \psi_i(\mathbf{r}) \tau_i(\xi). \quad (2)$$

Here, the wave functions  $\tau_i$  represent orthonormal eigenfunctions in the Hilbert space of the object and  $\psi_i = \langle \tau_i | \Psi \rangle$  are expansion coefficients depending on the probe electron degree of freedom  $\mathbf{r}$ , which we interpret as partial waves of the scattered electron. Measuring the probability density of the electron beam then consists of taking the absolute square of these waves and additionally integrating over all not observed object degrees of freedom  $\xi$ :

$$\rho_s(\mathbf{r}) = \sum_{ij} \psi_i(\mathbf{r}) \psi_j^*(\mathbf{r}) \langle \tau_j | \tau_i \rangle = \sum_i |\psi_i(\mathbf{r})|^2. \quad (3)$$

The measurement destroys the phase relation between these waves  $\psi_i$  leading to an incoherent summation of intensities. Consequently the state of the probe electron changes irreversibly from a pure to a mixed state, which cannot be described by a single wave function. This corresponds in general to a non-unitary evolution of the electron state from the object entrance plane to the object exit plane. It is then convenient to use a more comprehensive description of the quantum state comprising both pure and mixed states in one quantity, the density matrix defined as [19,20]:

$$\rho_s(\mathbf{r}, \mathbf{r}') = \sum_i \psi_i(\mathbf{r}) \psi_i^*(\mathbf{r}'). \quad (4)$$

Here,  $\rho_s$  denotes the reduced density matrix describing the state of the electron at the object exit plane. The term “reduced” indicates the integration over the internal object degrees of freedom as conducted in (3). The high convenience of the density matrix description now lends from the following observation. One can show that the any quantum mechanical expectation value of operators solely acting in the beam electron Hilbert space may be obtained from the density matrix without any knowledge about the entangled object. For instance, the diagonal elements of the density matrix (4) are proportional to the intensity of a pure/mixed state in the sense of (1). Furthermore, the off-diagonal elements describe the coherence of the probe electron state. The mixed state properties of the single probe electron introduced by inelastic interaction, i.e. probe electron–object entanglement, will be referred to as *state coherence* in the following (subscript  $s$ ). The state coherence is determined by electron–electron correlations

in the object convoluted with the delocalized Coulomb interaction [8]. Additionally the density matrix concept is useful to describe another important effect related to the whole statistical beam ensemble consisting of mutually incoherent electrons. Its coherence properties, introduced by statistical fluctuations of parameters like the electron energy or momentum, will be referred to as *ensemble coherence* on the other hand. The aim of this work is to separate the state coherence  $\rho_s$ , containing information about the object, from coherence properties of the beam electron ensemble.

We note that the density matrix is a representation of the density operator  $\hat{\rho}$  describing classical and quantum statistical properties of the electron beam. This means that intensity and coherence is not a general property of the electron beam, they rather depend on the concrete representation of the density operator. In position space, e.g. representing the object plane, we may write

$$\rho(\mathbf{r}, \mathbf{r}') = \langle \mathbf{r} | \hat{\rho} | \mathbf{r}' \rangle. \quad (5)$$

Inserting completeness relations for eigenfunctions of the lateral momentum operator  $\mathbf{I} = \int |\mathbf{q}\rangle \langle \mathbf{q}| d^2q$ , we obtain a basis transformation into Fourier space, which will be interpreted optically as back focal plane of an ideal lens (in paraxial approximation):

$$\begin{aligned} \rho(\mathbf{r}, \mathbf{r}') &= \int \langle \mathbf{r} | \mathbf{q} \rangle \langle \mathbf{q} | \hat{\rho} | \mathbf{q}' \rangle \langle \mathbf{q}' | \mathbf{r}' \rangle d^2q d^2q' \\ &= \int \rho(\mathbf{q}, \mathbf{q}') e^{2\pi i(\mathbf{q}\mathbf{r} - \mathbf{q}'\mathbf{r}')} d^2q d^2q' \\ &=: \text{FT}^{-1}[\rho(\mathbf{q}, \mathbf{q}')]. \end{aligned} \quad (6)$$

This is the definition of the inverse (symplectic) Fourier transformation for density matrices, which we will use throughout this paper.

The aim of the following subsections is to discuss influences of the ensemble coherence on the state coherence given by  $\rho_s$  in the transmission electron microscope. Throughout this paper we will not concern about the scattering process leading to  $\rho_s$ , which is layed out for instance in Refs. [16,9,25–27,23]. Here we focus on the transfer of  $\rho_s$  in TEM. For the sake of simplicity, we neglect the effect of image spread, which is not essential for this work but can be incorporated according to Ref. [11].

## 2.2. Electron source

For the case of TEM, we can assume the object plane to be located in the far field of the plane of the electron source. Due to this relationship we use position vectors  $(\mathbf{r}, \mathbf{r}')$  as coordinates for the object plane and spatial frequency vectors  $(\mathbf{k}_\perp, \mathbf{k}'_\perp)$  directly as coordinates for the source plane. We consider a poly-chromatic source with a finite lateral extension of emitting points  $\mathbf{k}_\perp$ . Each point yields the same normalized energy spectrum  $f_c(E)$  with an intensity given by  $f_s(\mathbf{k}_\perp)$ . We assume further that all emission points are mutually incoherent. For this case the density matrix describing the emitted electron beam at the source plane reads

$$\rho_b(\mathbf{k}_\perp, \mathbf{k}'_\perp, E) = f_c(E) f_s(\mathbf{k}_\perp) \delta(\mathbf{k}_\perp - \mathbf{k}'_\perp). \quad (7)$$

The spatial incoherence at the source plane is an approximation providing acceptable results with respect to coherence in the far field of the source. Here, we assume that the propagation of high energetic electrons (200 keV) into the far field of the source is independent on energy fluctuations in the order of 1 eV. Thus, we obtain the far field (i.e. in the object plane) by inverse Fourier transformation with respect to the lateral dimensions:

$$\rho_b(\mathbf{r}, \mathbf{r}', E) = \text{FT}^{-1}[\rho_b(\mathbf{k}_\perp, \mathbf{k}'_\perp, E)] = f_c(E) \tilde{f}_s(\mathbf{r} - \mathbf{r}'). \quad (8)$$

The two-dimensional vectors  $\mathbf{r}$  and  $\mathbf{r}'$  describe the lateral coordinates at the object plane. The tilde indicates the inverse Fourier transformation of  $f_s$ . In case of energy dependent propagation,  $\tilde{f}_s$  would become energy dependent, which is expected to be a negligible effect for usual distances in TEM. The absolute incoherence of the emitting source points leads to spatially homogeneous and parallel illumination conditions in the far field. However, real sources provide inhomogeneous illuminations due to finite spatial coherence at the source plane (beam aperture). In practical conventional TEM, the illumination is therefore adjusted such that only the homogeneous part of the beam near the optical axis contributes to the illuminated area. In this case, (8) is a useful approximation for the object illumination. Then, the degree of spatial coherence is determined through the quotient between off-diagonal and diagonal elements as

$$\mu(\mathbf{d}) = \frac{\int \rho_b(\mathbf{d}, E) dE}{\int \rho_b(0, E) dE} = \tilde{f}_s(\mathbf{d}). \quad (9)$$

Here, we integrate over the energy spectrum due to the measurement process. (9) reflects the well known van Cittert–Zernike theorem in optics [53,54] stating that the spatial coherence in the far field is determined through the Fourier transform of the normalized source distribution  $f_s$ . Note that the spatial extension of the source determines the illumination aperture in the object plane, i.e. the angular distribution of the incoming mutually incoherent plane waves. The effective spatial extension can be controlled through magnifying or demagnifying the source image located in the focal plane of the condenser lens.

## 2.3. Object

In the object plane the electron beam interacts with the object, which generally depends on incident angle and energy of the impinging electrons. However, in case of small illumination apertures in the order of 0.1 mrad and energy fluctuations  $E_c$  small compared to the kinetic energy of the beam, we can assume that **each incoming electron of the electron beam (8) is scattered in the same way, i.e. resulting in  $\rho_s(\mathbf{r}, \mathbf{r}', E)$** .  $E$  denotes a possible energy loss induced by various inelastic interactions. The off-diagonal elements of  $\rho_s$  determine the state coherence of the probe electron after interaction. The scattered electron beam at the object exit plane  $\rho_o$  is then given by

$$\begin{aligned} \rho_o(\mathbf{r}, \mathbf{r}', E) &= \int e^{2\pi i(\mathbf{q}\mathbf{r} - \mathbf{q}'\mathbf{r}')} f_s(\mathbf{k}_\perp) f_c(E_c) \\ &\quad \times \rho_s(\mathbf{q} - \mathbf{k}_\perp, \mathbf{q}' - \mathbf{k}'_\perp, E - E_c) d^2k_\perp dE_c d^2q d^2q' \\ &= \int \rho_b(\mathbf{r} - \mathbf{r}', E_c) \rho_s(\mathbf{r}, \mathbf{r}', E - E_c) dE_c \end{aligned} \quad (10)$$

**The convolution in energy space restricts the energy resolution in electron energy loss spectroscopy (EELS).** The off-diagonal elements of  $\rho_o$  additionally contain the spatial ensemble coherence of the electron beam generally dampening its state coherence. Here, we conclude that the experimental reconstruction of  $\rho_s$  at a limited signal-to-noise ratio requires an acceptable degree of coherence with suitable electron current density, which can only be realized by high-brightness electron guns [55].

## 2.4. Objective lens

Isoplanatic aberrations of the objective lens can be described as phase shifts through the wave aberration function  $\chi(\mathbf{q}, E)$  at the back focal plane. The wave aberration depends on energy in particular leading to different foci at different kinetic energies of the electrons, which is referred to as the chromatic aberration. These wave aberrations affect the object plane density matrix

$\rho_o(\mathbf{r}, \mathbf{r}', E)$  by multiplication of the wave transfer function (WTF)

$$\text{WTF}(\mathbf{q}, \mathbf{q}', E) = e^{-i(\chi(\mathbf{q}, E) - \chi(\mathbf{q}', E))} \quad (11)$$

at the back focal plane [16]. In the absence of energy filters, we additionally integrate over the energy loss  $E$  suffered by inelastic interaction of the object and obtain

$$\rho_{fp}(\mathbf{q}, \mathbf{q}') = \int \rho_s(\mathbf{q} - \mathbf{k}_\perp, \mathbf{q}' - \mathbf{k}_\perp, E) f_s(\mathbf{k}_\perp) d^2 k_\perp \times \int f_C(E_c) \text{WTF}(\mathbf{q}, \mathbf{q}', E + E_c) dE_c dE. \quad (12)$$

Here, the spatial coherence induces a blurring of the momentum space density matrix, while the temporal coherence dampens the off-diagonal elements only. **The latter is responsible for fringe contrast damping in CBED holography** (e.g. [56]) and has to be taken into account for quantitative interpretations. A conventional intensity measurement at the back focal plane would yield the diffraction pattern:

$$I_{fp}(\mathbf{q}) = \int \rho_s(\mathbf{q} - \mathbf{q}_0, \mathbf{q} - \mathbf{q}_0, E) f_s(\mathbf{q}_0) d^2 q_0 dE. \quad (13)$$

The limited ensemble coherence blurs the diffraction pattern by convolution with the source distribution function  $f_s$ , while it does not limit the range of transferred  $\mathbf{q}$  vectors.

### 2.5. Image plane

The image plane density matrix  $\rho_i$  is obtained from (12) after a subsequent inverse Fourier transformation:

$$\rho_i(\mathbf{r}, \mathbf{r}') = \int e^{2\pi i(\mathbf{q}\mathbf{r} - \mathbf{q}'\mathbf{r}')} \text{WTF}(\mathbf{q}, \mathbf{q}', E + E_c) \rho_s(\mathbf{q} - \mathbf{k}_\perp, \mathbf{q}' - \mathbf{k}_\perp, E) \times f_s(\mathbf{k}_\perp) f_C(E_c) d^2 k_\perp dE_c d^2 q d^2 q' dE. \quad (14)$$

Using the coordinate transformations  $\mathbf{q} - \mathbf{k}_\perp \rightarrow \mathbf{q}$  and  $\mathbf{q}' - \mathbf{k}_\perp \rightarrow \mathbf{q}'$  in the usual way [2], we can express the density matrix at the image plane by

$$\rho_i(\mathbf{r}, \mathbf{r}') = \int e^{2\pi i(\mathbf{q}\mathbf{r} - \mathbf{q}'\mathbf{r}')} \text{TCC}(\mathbf{q}, \mathbf{q}', \mathbf{r} - \mathbf{r}', E) \rho_s(\mathbf{q}, \mathbf{q}', E) d^2 q d^2 q' dE. \quad (15)$$

Consequently, the integration of the WTF over the beam ensemble parameters  $(\mathbf{k}_\perp, E_c)$  yields the transmission cross-coefficient [2] in a generalized form indicated by the additional  $\mathbf{d} = \mathbf{r} - \mathbf{r}'$  dependency:

$$\text{TCC}(\mathbf{q}, \mathbf{q}', \mathbf{d}, E) = \int e^{2\pi i \mathbf{k}_\perp \mathbf{d}} \text{WTF}(\mathbf{q} + \mathbf{k}_\perp, \mathbf{q}' + \mathbf{k}_\perp, E + E_c) \times f_s(\mathbf{k}_\perp) f_C(E_c) d^2 k_\perp dE_c. \quad (16)$$

This generalized TCC incorporates the effect of spatial coherence of the incident electron beam ensemble on the diagonal and off-diagonal elements of the beam electron density matrix at the image plane correctly. The dependency on  $\mathbf{d} = \mathbf{r} - \mathbf{r}'$  is necessary to discuss the density matrix at the detection plane rather than intensities only ( $\mathbf{d} = 0$ ). **In the absence of objects**, i.e.  $\rho_s(\mathbf{q}, \mathbf{q}', E) = \delta(\mathbf{q})\delta(\mathbf{q}')\delta(E)$ , the influence of the generalized TCC in (15) reduces to

$$\text{TCC}(0, 0, \mathbf{d}, E) = \int e^{2\pi i \mathbf{k}_\perp \mathbf{d}} f_s(\mathbf{k}_\perp) f_C(E_c) d^2 k_\perp dE_c. \quad (17)$$

This expression is equivalent to the degree of coherence defined in (9) and solely describes the spatial coherence of the electron beam.

A conventional TEM image recorded in the image plane corresponds to the diagonal elements of (15). Thus, the intensity

is given by

$$I_i(\mathbf{r}) = \int e^{2\pi i(\mathbf{q} - \mathbf{q}')\mathbf{r}} \text{TCC}(\mathbf{q}, \mathbf{q}', 0, E) \rho_s(\mathbf{q}, \mathbf{q}', E) d^2 q d^2 q' dE. \quad (18)$$

Here, the intensity distribution becomes blurred by bi-convolution of the density matrix with the TCC. Consequently, the Fourier spectrum of (18) yields the known expression for the cross-correlation of the density matrix weighted by the transmission cross-coefficient:

$$I_i(\mathbf{q}) = \int \text{TCC}(\mathbf{q} + \mathbf{q}', \mathbf{q}', 0, E) \rho_s(\mathbf{q} + \mathbf{q}', \mathbf{q}', E) d^2 q' dE. \quad (19)$$

Compared to the measured intensity at the back focal plane (13), the range of transferred  $\mathbf{q}$  vectors (19) is limited by incoherent aberrations of the objective lens. This discussion shows that measurements in both image and back focal planes can be brought into a consistent picture only by regarding the density matrix transfer. This aspect remains still an open topic for the theoretical background of electron diffractive imaging techniques. Furthermore, this explains among others the degradation of lattice contrast especially in energy filtered TEM images (EFTEM) by defocussing due to strongly reduced spatial coherence through inelastic interaction. In the following we concentrate on the case of off-axis electron holography and derive the according transfer theory.

### 3. Holographic transfer theory for the density matrix

In off-axis electron holography (EH) a Möllenstedt biprism [36] is usually mounted between the back focal plane of the objective and the first image plane (Fig. 1). This biprism splits and inclines the transmitted wave fronts towards each other. Propagation into the image plane leads to the formation of interference fringes locally altered in contrast and bending. In dependence on the biprism voltage, positions separated by the shear  $d$  in the object plane are related with each other in the image plane. Fresnel diffraction at the biprism rim plays a crucial role in the fringe

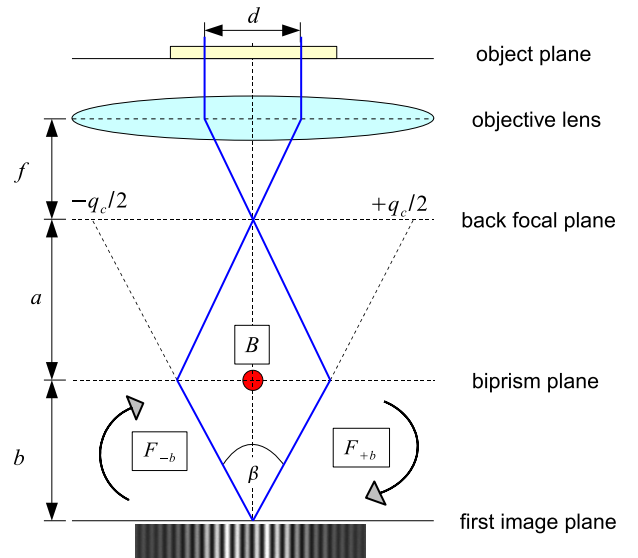


**Fig. 1.** Schematic drawing of the electron ray paths as realized in off-axis electron holography. Two trajectories (blue) separated by the shear  $d$  at the object plane superimpose at the image plane due to deflection in the electric field of the positively charged Möllenstedt biprism (red). The interfering rays are inclined by the angle  $\beta$  towards each other creating a cosinoidal fringe pattern with the carrier frequency  $q_c$  according to (22). The formation of the fringe pattern can be described by backward Fresnel propagation from the image plane to the biprism plane by  $F_{-b}$  (24), application of the biprism operator  $B$  (20) and forward Fresnel propagation by  $F_{+b}$  (24) downwards to the image plane. (For interpretation of the references to colour in this figure legend, the reader is referred to the web version of this paper.)



pattern formation and was already addressed in [45]. The influence of the biprism in case of limited spatial coherence, however, was not completely investigated. Therefore we derive a general transfer theory for the density matrix in case of off-axis electron holography.

### 3.1. The Möllenstedt biprism

We approximate the action of the biprism as an amplitude and phase modulation in a plane, which is Fresnel defocussed with respect to the image plane. According to Refs. [45,22,57], this wave modulation, i.e. splitting and inclining the wave fronts, may be described by an operator, here called  $B(\mathbf{q}, \mathbf{q}')$  in Fourier space representation. We assume an energy dispersion of the biprism small compared to the corresponding deflection angles. This is valid at typical electron acceleration voltages in the range of 80–300 keV and beam energy widths in the order of 1 eV. Therefore the biprism operator does not depend on energy. Assuming a biprism diameter  $D$  and a carrier frequency  $\mathbf{q}_c$  of the fringe pattern, we express the biprism operator as a modulation function for the electron beam density matrix:

$$B(\mathbf{q}, \mathbf{q}') = \int H_D\left(\frac{\mathbf{q}_c \mathbf{r}}{q_c}\right) H_D^*\left(\frac{\mathbf{q}_c \mathbf{r}'}{q_c}\right) \times e^{-i\pi(\mathbf{q}_c \mathbf{r} - \mathbf{q}_c \mathbf{r}') \cdot \mathbf{q}_c} e^{-2\pi i(\mathbf{q} \mathbf{r} - \mathbf{q}' \mathbf{r}') \cdot \mathbf{q}_c} d^2 r d^2 r'. \quad (20)$$

The function  $H_D$  describes the shadowing of the wave field over the width  $D$  in the biprism direction and is here defined as

$$H_D(a) := \begin{cases} 0 & \text{for } |a| \leq D/2 \\ 1 & \text{for } |a| > D/2. \end{cases} \quad (21)$$

The absolute values in (20) are responsible for the different signs of the phase wedges around the biprism required for the inclination of the waves fields towards each other. The vector  $\mathbf{q}_c$  determines the slope of these phase wedges and is related to the inclination angle  $\beta$  of the interfering waves by (small angle approximation)

$$\beta = \frac{q_c}{k_0}. \quad (22)$$

As depicted in Fig. 1, the biprism action can be incorporated by Fresnel back propagation of the image plane density matrix (15) into the biprism plane at distance  $b$  above the image plane. After application of  $B(\mathbf{q}, \mathbf{q}')$  on the density matrix, propagation of this result into the image plane yields the density matrix modulated by the Möllenstedt biprism.

In the following, we refer all geometric quantities to the object plane (subscript  $o$ ). Consequently, the propagation along  $b$  corresponds to a virtual propagation along  $b_o$  with

$$b_o = \frac{b}{MM_B} = \frac{bf^2}{a(a+b)}. \quad (23)$$

Here,  $f$  denotes the focal length of the objective and  $a$  denotes the distance between the back focal plane and the biprism plane.  $M$  describes the reproduction scale between image and object plane and  $M_B$  relates biprism plane and virtual biprism plane above the object. Fresnel propagation of the image density matrix  $\rho_i$  by a length  $b_o$  is given by the Fresnel propagator (expressed in Fourier space):

$$F_{b_o}(\mathbf{q}, \mathbf{q}') = e^{-i\pi(b_o/k_0)(\mathbf{q}^2 - \mathbf{q}'^2)}. \quad (24)$$

Here,  $b_o > 0$  corresponds to the forward propagation downwards the TEM column. Applying the backward and forward propagation and the biprism operator in between, we end up with the following expression of the holographic density matrix  $\rho_h$

at the image plane:

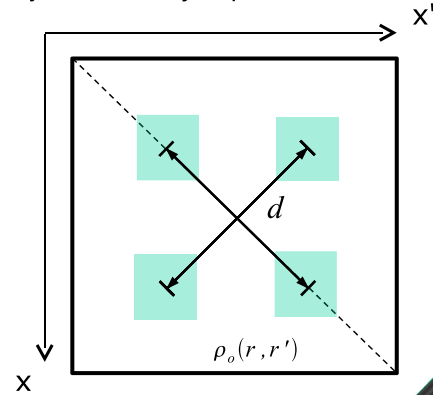
$$\rho_h(\mathbf{r}, \mathbf{r}') = \int \rho_i(\mathbf{q}_1, \mathbf{q}'_1) F_{-b_o}(\mathbf{q}_1, \mathbf{q}'_1) B(\mathbf{q}_2 - \mathbf{q}_1, \mathbf{q}'_2 - \mathbf{q}'_1) d^2 q_1 d^2 q'_1 \times F_{+b_o}(\mathbf{q}_2, \mathbf{q}'_2) e^{2\pi i(\mathbf{q}_2 \mathbf{r} - \mathbf{q}'_2 \mathbf{r}')} d^2 q_2 d^2 q'_2. \quad (25)$$

With respect to the density matrix at the object plane, this complex operation can be understood in the sense of Fig. 2. Due to interference of rays separated by the shear  $\mathbf{d}$ , different areas of the object density matrix  $\rho_o$  become correlated and will be superimposed at the image plane leading to  $\rho_h$ . The intensity measurement by a CCD-camera provides access to the diagonal elements of  $\rho_h$  only. This intensity distribution consists of an interference fringe pattern, which is formed by contributions from the diagonal elements of  $\rho_o$ , the so called centre bands, and from the off-diagonal elements, the so called sidebands. The latter are of particular interest for the reconstruction of the density matrix at the object plane.

### 3.2. The holographic TCC

Since we are ultimately interested in the state coherence density matrix  $\rho_o$ , containing the object properties, we have to insert (14) into (25) and integrate over the beam ensemble parameters. Eventually we obtain for the hologram intensity,

Density matrix at object plane:



Density matrix at image plane:

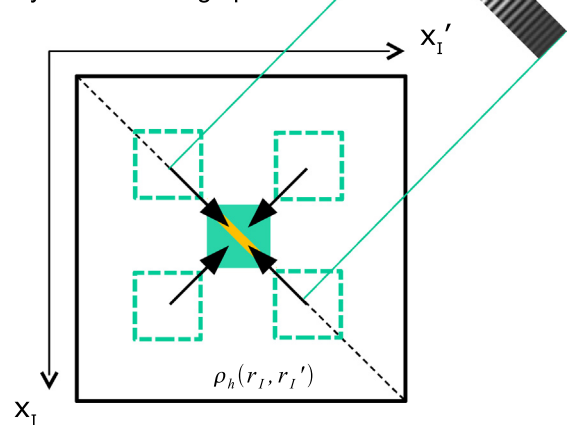


**Fig. 2.** Top: One-dimensional density matrix at the object plane: The biprism correlates different positions in the wave field, which are separated by  $d$  within the object plane. The green squares denote the areas, which contribute to the holographic density matrix in the centre of the image plane (bottom: darker greened square). These parts of the object plane density matrix superimpose to form a measurable interference fringe pattern on the main diagonal. (For interpretation of the references to colour in this figure legend, the reader is referred to the web version of this paper.)

i.e. the diagonal elements of (25), at the image plane:

$$I_h(\mathbf{r}) = \int \rho_s(\mathbf{q}_1, \mathbf{q}'_1, E) \text{TCC}_h(\mathbf{q}_1, \mathbf{q}'_1, \mathbf{q}_2 - \mathbf{q}'_2, E) F_{-b_o}(\mathbf{q}_1, \mathbf{q}'_1) B(\mathbf{q}_2 - \mathbf{q}_1, \mathbf{q}'_2 - \mathbf{q}'_1) \\ \times F_{+b_o}(\mathbf{q}_2, \mathbf{q}'_2) e^{2\pi i(\mathbf{q}_2 - \mathbf{q}'_2) \cdot \mathbf{r}} d^2 q_1 d^2 q'_1 d^2 q_2 d^2 q'_2 dE \quad (26)$$

Here, we introduce the holographic transmission cross-coefficient  $\text{TCC}_h$  including the effect of partial coherence on the biprism action. The  $\text{TCC}_h$  is defined as

$$\text{TCC}_h(\mathbf{q}_1, \mathbf{q}'_1, \mathbf{q}_2 - \mathbf{q}'_2, E) \\ := \int f_s(\mathbf{k}_\perp) f_c(E_c) \text{WTF}(\mathbf{q}_1 + \mathbf{k}_\perp, \mathbf{q}'_1 + \mathbf{k}_\perp, E + E_c) \\ \times e^{2\pi i(b_o/k_o)(\mathbf{q}_1 - \mathbf{q}'_1) \cdot \mathbf{k}_\perp} e^{-2\pi i(b_o/k_o)(\mathbf{q}_2 - \mathbf{q}'_2) \cdot \mathbf{k}_\perp} d^2 k_\perp dE_c. \quad (27)$$

The holographic TCC determines the spatial and temporal coherence in the presence of aberrations through an objective lens and the biprism. The biprism influence is mainly determined by the object related distance between biprism and image plane ( $b_o$ ). Its main influence depends on illumination aperture  $\mathbf{k}_\perp$  and propagation length  $b_o$  and becomes obvious by the attenuation of high spatial frequency contributions of the Fresnel fringes formed at the image plane.

For the special case  $\mathbf{q}_2 - \mathbf{q}'_2 = \mathbf{q}_1 - \mathbf{q}'_1 - \mathbf{q}_c$ , the holographic TCC can be reduced to the generalized TCC (16) in the following way:

$$\text{TCC}(\mathbf{q}_1, \mathbf{q}'_1, \mathbf{d}, E) = \text{TCC}_h(\mathbf{q}_1, \mathbf{q}'_1, \mathbf{q}_1 - \mathbf{q}'_1 - \mathbf{q}_c, E). \quad (28)$$

Here, the vector  $\mathbf{q}_c$  denotes the carrier frequency of the fringe pattern, which depends on the shear between the interfering beams:

$$\mathbf{d} = \frac{\mathbf{q}_c}{k_o}. \quad (29)$$

It will turn out that in case of off-axis electron holography, the relation (28) is very useful. In the following we will decompose the holographic fringe pattern in four terms, i.e. two centre and two sideband terms. We will see that the holographic TCC describes both the information transfer into centre band and sideband completely.

### 3.3. Interpretation of centre and sideband

As outlined in Appendix B we decompose the expression (26) into centre and sideband:

$$I_h(\mathbf{r}) = \rho^{+\mp} \left( \mathbf{r} + \frac{\mathbf{d}}{2}, \mathbf{r} \pm \frac{\mathbf{d}}{2} \right) + \rho^{-\pm} \left( \mathbf{r} - \frac{\mathbf{d}}{2}, \mathbf{r} \pm \frac{\mathbf{d}}{2} \right) \\ + \rho^{+\pm} \left( \mathbf{r} + \frac{\mathbf{d}}{2}, \mathbf{r} \pm \frac{\mathbf{d}}{2} \right) e^{-2\pi i \mathbf{q}_c \cdot \mathbf{r}} \\ + \rho^{-\mp} \left( \mathbf{r} - \frac{\mathbf{d}}{2}, \mathbf{r} \pm \frac{\mathbf{d}}{2} \right) e^{+2\pi i \mathbf{q}_c \cdot \mathbf{r}}. \quad (30)$$

This expression corresponds to the cosinoidal fringe pattern observed in off-axis electron holography. The first two terms form the centre band by the diagonal element of the density matrices  $\rho^{+\mp}$  and  $\rho^{-\pm}$  shifted by  $\mathbf{d}/2$  towards each other. We employed a tilde symbol to indicate the corresponding signs in the expressions to reduce the length of the following formula. The last two terms in (30) determine the sidebands and – as suggested by notation – are represented by off-diagonal elements of the density matrices  $\rho^{+\pm}$  and  $\rho^{-\mp}$  respectively. Again, these elements are shifted by the shear vector  $\mathbf{d}/2$  on the main diagonal of the density matrix at the image plane. In this summarizing notation we find for the corresponding density matrices:

$$\rho^{\pm\pm} \left( \mathbf{r} \pm \frac{\mathbf{d}}{2}, \mathbf{r} \pm \frac{\mathbf{d}}{2} \right) \\ = \int \rho_s(\mathbf{q}_1, \mathbf{q}'_1, E) \text{TCC}_h \left( \mathbf{q}_1, \mathbf{q}'_1, \mathbf{q}_2 \mp \frac{\mathbf{q}_c}{2} - \mathbf{q}'_2 \pm \frac{\mathbf{q}_c}{2}, E \right) \\ \times F_{-b_o}(\mathbf{q}_1, \mathbf{q}'_1) H_{D_o \pm}(\mathbf{q}_2 - \mathbf{q}_1) H_{D_o \pm}^*(\mathbf{q}'_2 - \mathbf{q}'_1) F_{+b_o}(\mathbf{q}_2, \mathbf{q}'_2)$$

$$\times e^{2\pi i(\mathbf{q}_2(\mathbf{r} \pm \mathbf{d}/2) - \mathbf{q}'_2(\mathbf{r} \pm \mathbf{d}/2))} d^2 q_1 d^2 q'_1 d^2 q_2 d^2 q'_2 dE. \quad (31)$$

The expressions (30) and (31) completely describe the transfer of the probe electron density matrix  $\rho_s$  into the centre and sidebands of an off-axis electron hologram. In our notation that corresponds to virtually placing a biprism with diameter  $D_o$  at a distance  $b_o$  above the object, which is excited to produce an interference pattern with carrier frequency  $\mathbf{q}_c$  in the object plane. The latter corresponds to a shear of  $\mathbf{d}$  according to (29).

Eq. (31) indicates that the centre and sideband are differently affected by the aberrations of the objective lens and the biprism, which was worked out before for special cases (e.g. [10,50,59]). This becomes obvious in the  $\mathbf{q}_c$  dependency of the holographic TCC, which vanishes only for the centre band ( $\rho^{+\mp} + \rho^{-\pm}$ ) but not for the sidebands ( $\rho^{+\pm}$  and  $\rho^{-\mp}$ ). To demonstrate the validity of the derived formula, we reproduce the known transfer formula for off-axis electron holography with elastically scattered electrons as a special case in Appendix C.

## 4. Reconstruction of the density matrix

In the following subsection we present a principal procedure for acquiring the data necessary for reconstructing the density matrix. Since the measured fringe pattern (30) and (31) is related to the state coherence density matrix  $\rho_s$  at the object plane in a complicated manner, we derive in the next subsection conditions simplifying the transfer formula. In the final subsection we verify these conditions by numerical simulations.

### 4.1. The measurement principle

Since the (energy integrated) density matrix of the probe electron at the object plane is a four-dimensional quantity, a single interference pattern, i.e. a two-dimensional intensity distribution, is not sufficient to reconstruct the complete density matrix. Only off-diagonal elements separated by  $\mathbf{d}/2$  from the diagonal elements will contribute. To access all off-diagonal elements a set of interference patterns obtained from varying the shear  $\mathbf{d}$  (biprism voltage) has to be acquired. This has to be conducted for two (preferably orthogonal) biprism orientations to access all off-diagonal elements. A single measurement corresponds to a projection of the density operator onto distinguished basis functions. In case of ideal information transfer (i.e.  $\text{TCC}_h = 1$  and  $H_{D_o \pm}(\mathbf{q}) = \delta(\mathbf{q})$  in (31)), these basis functions would correspond to eigenfunctions of the 2D position operator at the object exit plane, thus the expression (31) can be formally written as

$$\hat{\rho}_s \rightarrow \rho^{\pm\pm} \left( \mathbf{r} \pm \frac{\mathbf{d}}{2}, \mathbf{r} \pm \frac{\mathbf{d}}{2} \right) = \left\langle \mathbf{r} \pm \frac{\mathbf{d}}{2} \left| \hat{\rho}_s \right| \mathbf{r} \pm \frac{\mathbf{d}}{2} \right\rangle. \quad (32)$$

In this highly simplified case, the sampling of the two-dimensional shear space would directly yield the quantum state  $\hat{\rho}_s$  in position space representation. However, as demonstrated here, the information transfer of a transmission electron microscope is by far not ideal, thus (32) is not valid in general. Therefore, we investigate in the next subsection, under which assumption the projection (32) is a suitable approximation for (31).

### 4.2. Direct density matrix reconstruction

The relation between the acquired intensity and the reduced density matrix of the probe electron (30) and (31) is too complex for directly reconstructing the state coherence. For convenience we deliberately orient the biprism in the y-direction in the following. The main obstacle is the coupling between the holographic TCC and the Fresnel diffraction at the biprism in (31).

However, a decoupling of the Fresnel diffraction and the transfer properties of the conventional TEM can be achieved as outlined in [Appendix D](#), if the combined angular width perpendicular to the biprism consisting of the illumination aperture ( $k_{\perp x}/k_0$ ) and of the scattering process ( $q_{1x}/k_0$ ) is small in the following sense:

$$\frac{|q_{1x} + k_{\perp x}|}{k_0} \ll \frac{1}{b_0} \left( \frac{d - D_0}{2} \right). \quad (33)$$

The parameters on the right hand side solely depend on the geometry (23) and voltage (29) of the biprism. This relation implies that the shear is lower limited by the biprism diameter. Due to homogeneity in the direction of the biprism, the

integration of the  $y$ -component of  $\mathbf{q}_2$  yields 1, thus the condition for separation of Fresnel diffraction only contains components of the wave vector perpendicular to the biprism. If (33) holds true, (31) simplifies for the axial region of the fringe pattern ( $x \ll (d - D_0)/2$ ), to (D.10) as outlined in [Appendix D](#). A further simplification can be achieved when considering homogeneous objects (subscript H) possessing a diagonalized density matrix at the back focal plane:

$$\rho_s(\mathbf{q}, \mathbf{q}', E) = \rho_{sH}(\mathbf{q}, E) \delta(\mathbf{q} - \mathbf{q}'). \quad (34)$$

The function  $\rho_{sH}(\mathbf{q}, E)$  simply describes the angular scattering distribution as a function of energy loss  $E$ . Assuming homogeneity

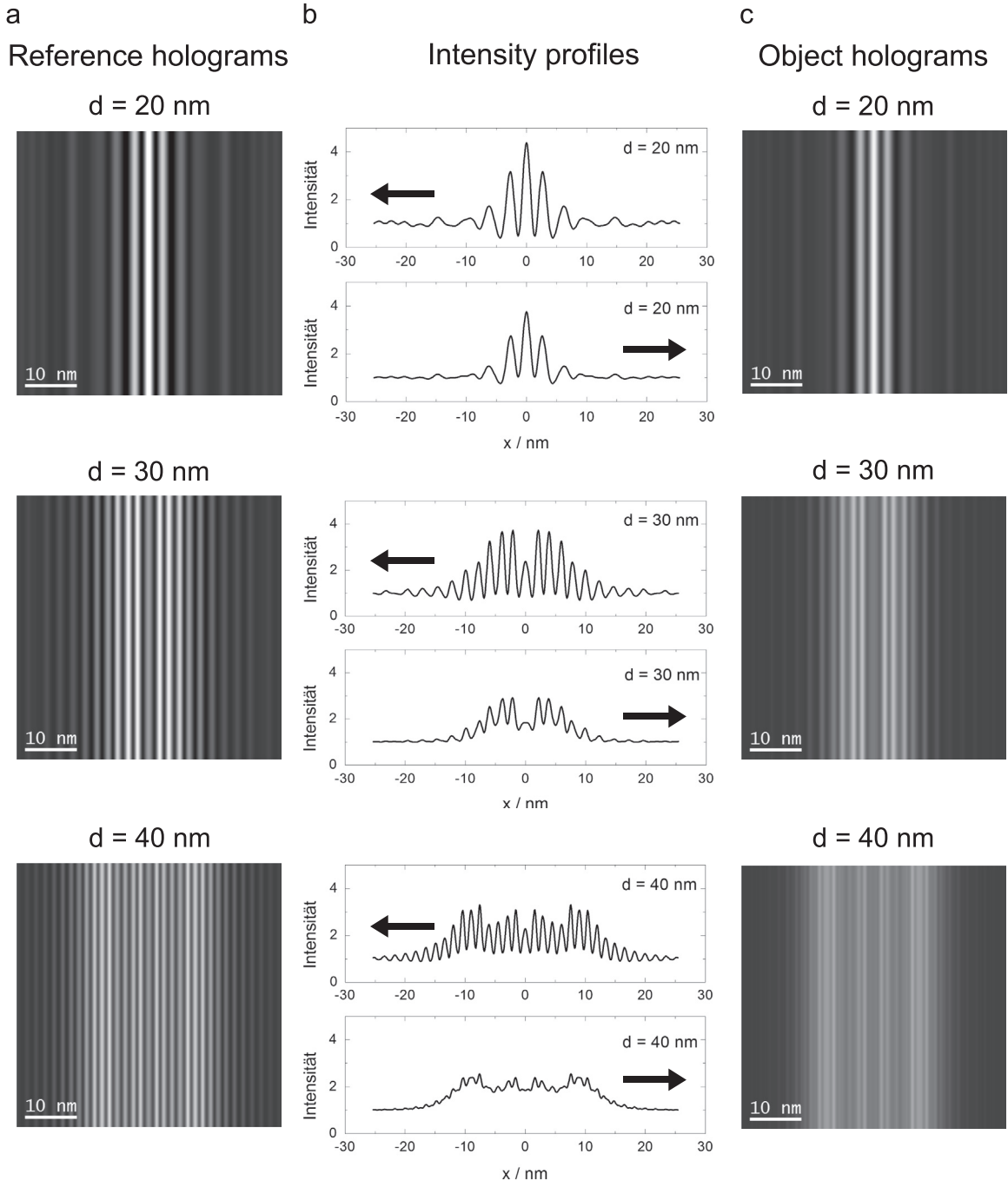


**Fig. 3.** Fringe pattern calculated from exact transfer theory (30) and (31) in the absence of an object (a) and with homogeneous object (c) according to (37) with  $\sigma = 30$  nm for different shears:  $d = 20$  nm (1),  $d = 30$  nm (2) and  $d = 40$  nm (3). The corresponding profiles are shown in (b).

further simplifies the modulation function for the fringe pattern intensity (D.10) as follows:

$$\rho^{\pm} \left( \mathbf{r} \pm \frac{\mathbf{d}}{2}, \mathbf{r} \pm \frac{\mathbf{d}}{2} \right) \approx \underbrace{D_{\pm} \left( \mathbf{r} \pm \frac{\mathbf{d}}{2} \right)}_{\text{Fresnel diffraction}} \underbrace{D_{\pm}^* \left( \mathbf{r} \pm \frac{\mathbf{d}}{2} \right)}_{\text{ensemble coherence}} \underbrace{\text{TCC} \left( 0, 0, \pm \frac{\mathbf{d}}{2}, \pm \frac{\mathbf{d}}{2}, 0 \right)}_{\text{state coherence}} \rho_{\text{SH}} \left( \pm \frac{\mathbf{d}}{2}, \pm \frac{\mathbf{d}}{2} \right). \quad (35)$$

The functions  $D_{\pm}$  given by (D.9) describe the Fresnel diffraction at the biprism and are multiplied with the product of the probe electron density matrix and the TCC. For homogeneous objects, the TCC becomes independent of energy and spatial frequency. Thus, energy- and  $q$ -integration can be directly conducted leading to the state coherence term in (35).  $D_{\pm}$  only depends on the virtual biprism diameter  $D_o$ , propagation length  $b_o$  between the biprism plane virtually located above the object plane and on the shear  $\mathbf{d}$  w.r.t. the object plane. The term “virtual” means that these quantities refer to the object plane. The probe electron state coherence and the partial coherence of the electron beam dampens the holographic fringe pattern (30) for given shear as constant factors. The strategy for determination of  $\rho_{\text{SH}}$  from experimental measurements would then be to fit the general fringe pattern formula (30) using the above approximations (35) with the degree of coherence  $\mu$  (9):

$$\mu(\mathbf{d}) = \frac{\rho_{\text{SH}}(\mathbf{d})}{\rho_{\text{SH}}(0)} \cdot \text{TCC}(0, 0, \mathbf{d}, 0) \quad (36)$$

A reference measurement without object, i.e.  $\rho_{\text{SH}}(\mathbf{d}) = 1$ , is additionally necessary to determine the degree of partial coherence of the electron beam (TCC). A repetition of this procedure for all shears would then yield the density matrix in position space of a homogeneous object, with the following restrictions. The small angle condition (33) gets violated at small shear angles and, as indicated in (29), large shears increase the carrier frequency  $\mathbf{q}_c$  of the fringe pattern (30), thus undersampling may become a limiting experimental problem. In the following subsection we will numerically test this strategy by defining a model density matrix  $\rho_{\text{SM}}$ , which we subsequently extract from a simulated interference fringe series based on exact transfer theory (31) by using the approximation (35).

#### 4.3. Test of the small angle approximation

To test the validity of our approximation (35) we use a model density matrix of an electron scattered by a homogeneous fictitious object:

$$\rho_{\text{SM}}(\mathbf{r} - \mathbf{r}') = e^{-((\mathbf{r} - \mathbf{r}')/\sigma)^2}. \quad (37)$$

This gaussian function is shift invariant and depends only on the parameter  $\sigma$ , which can be interpreted as a “width of coherence” determined, e.g. by a fictitious inelastic small-angle scattering process. We will deliberately set  $\sigma = 30$  nm and calculate the expected fringe pattern for different shears using the exact transfer theory (30) and (31). The influence of the microscope is characterized by the parameters acceleration voltage  $U_A = 200$  kV and the focal length of the objective lens  $f = 2.9$  mm. Since the energy spread of the electron beam does not affect the density matrix of the homogeneous case, the only illumination characteristic is the illumination aperture of  $\vartheta = 20$   $\mu$ rad (indirection perpendicular to the biprism) at the object plane. This very small angular width is realized in off-axis electron holography by an elliptically shaped illumination with the large principal axis perpendicular to the biprism. That ensures acceptable partial coherence in this direction in combination with sufficient current

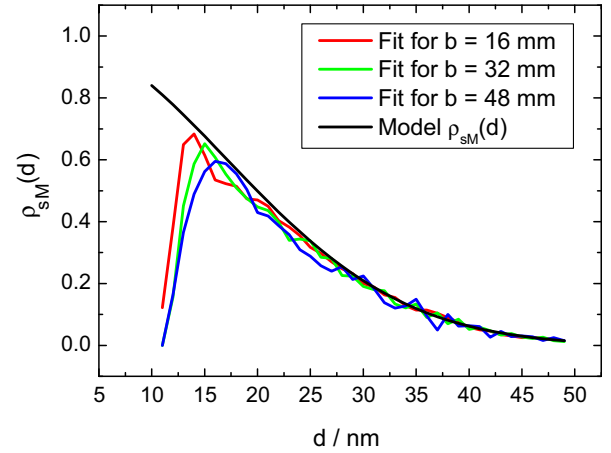


**Fig. 4.** Comparison of fitted density matrices (homogeneous case) to the underlying Gaussian-shaped model function (37): Different propagation lengths  $b$  were used to simulate differently formed fringe pattern:  $b = 16$  mm (red),  $b = 32$  mm (green) and  $b = 48$  mm (blue). (For interpretation of the references to colour in this figure legend, the reader is referred to the web version of this paper.)

density. The location of the biprism is  $a = 120$  mm below the back focal plane and  $b = 40$  mm above the first image plane. The physical diameter of the biprism is about  $D = 400$  nm. In Fig. 3 the calculated interference fringe patterns are presented for different shears as well as in the absence and presence of an object. For increasing shear a stronger attenuation is observable due to limited spatial coherence of the electron beam and additional fictitious inelastic scattering in the above-mentioned way. The contrast dampening is caused by the influence of different off-diagonal elements of the according density matrices to the formation of the fringe pattern (Fig. 2).

We now fit approximated fringe patterns according to (30) and (35) to the calculated fringe pattern series varying shear (three individual pairs of these series depicted above) and propagation length  $b$  (a key parameter in relation (33)). The non-linear fit was conducted using a Levenberg–Marquardt algorithm implemented in Matlab<sup>®</sup>. The degree of coherence (36) serves here as fitting parameter. From that, the ratios of the degrees of coherence with (Fig. 3c) and without (Fig. 3a) object yield the desired state coherence after scattering at the homogeneous object. In Fig. 4 the fitted results are compared to the underlying input according to (37). For a large range of shear values good agreement between fitted and expected values is observable. Deviations for smaller shears ( $10 \text{ nm} < d < 15 \text{ nm}$ ) are due to violating condition (33) necessary for the approximation (35). The observed  $b$  dependency further supports this finding: For a large  $b$  (blue curve) the condition is violated for larger shears, whereas a small  $b$  (red, green curve) allows a reconstruction for smaller shears. In any case, the finite width of the biprism  $D$ , leading to a virtual shadow at the object plane of  $D_o = D/M \approx 10$  nm, prohibits a reconstruction of off-diagonal elements for shears with  $d < D_o$  (see strong deviation around  $d = 10$  nm in Fig. 4).

From these model calculations, we conclude that it is possible to reconstruct off-diagonal elements of the reduced probe electron density matrix. The results are reliable for shears larger than the virtual diameter of the biprism  $D_o$ . In a second step we want to apply this transfer theory to experimental results. However, a homogeneous density matrix in position space is diagonal in Fourier space. That means, a single intensity measurement (with and without object) at the back focal plane would fully describe the density matrices at all planes below the object. The here presented method is more interesting for inhomogeneous objects, which cannot be fully described by a single measurement at the



back focal plane. As example we consider electrons aloofly scattered by a planar surface in the following section.

### 5. Experiment with Aloof beam electrons

The above discussion showed that a direct determination of the density matrix by inverting (31) is generally not possible. However for objects providing small-angle scattering in the direction perpendicular to the biprism (33), the transfer formula can be simplified (D.10) by separating the Fresnel diffraction terms.

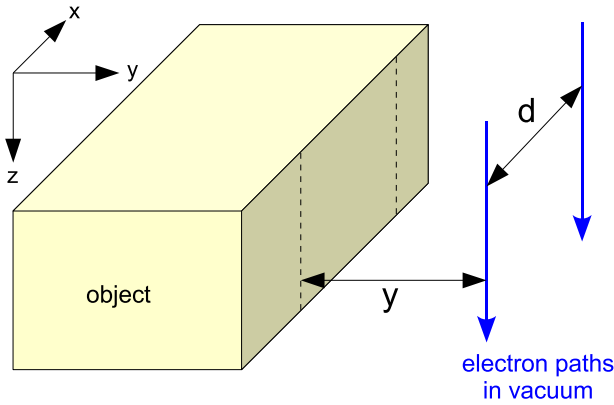


**Fig. 5.** Sketch of the experimental set-up in the object plane of the TEM. The trajectories interfering at the image plane are separated by the shear  $\mathbf{d}$  determined by the filament voltage of the biprism. Here, the biprism is orientated precisely in the  $y$ -direction, i.e. interfering paths have equal distance to the object.

Electrons penetrating the object, however, are elastically scattered to high-angles. In this regime, the condition (33) is valid only for shear values exceeding the coherence widths of inelastically scattered electrons by far. Thus in this case, the density matrix for the small angle scattered electrons can only be reconstructed using the exact transfer formula (31), which is difficult as mentioned above. This problem does not occur in case of aloof beam electrons exciting the object from vacuum. The electrons experience inelastic scattering only due to the delocalized Coulomb interaction screened by the dielectric response of the object.

A suitable set-up for this experiment is shown in Fig. 5. Here, we orient the biprism exactly perpendicular to the surface, i.e. the shear vector  $\mathbf{d}$  has only a component parallel to the surface. Thereby, we superimpose trajectories with the same distance to the object. Since, in this case, homogeneity is given in the normal direction to the biprism only, the separation of the density matrix  $\rho_s$  from the TCC (35) holds not true in general. Therefore we analyze in Appendix E the influence of semi-homogeneity on the coherence transfer in (D.10) before discussing experimental results. These considerations show that the dampening of fringe contrast parallel to the surface is only influenced by the inelastically scattered aloof electrons. Elastic high-angle and inelastic small-angle scattering in the  $y$ -direction do not introduce artefacts affecting the fringe pattern evaluation in the  $x$ -direction. Thus the main contribution to the fringe pattern is small angle scattering and partial coherence of the illumination both in the normal direction to the biprism.

As a suitable object for the aloof beam experiment, we cleaved a 500  $\mu\text{m}$  thick silicon waver to obtain a clean planar surface and oriented that parallel to the electron beam. Subsequently we applied four different voltages to the biprism and acquired the interference

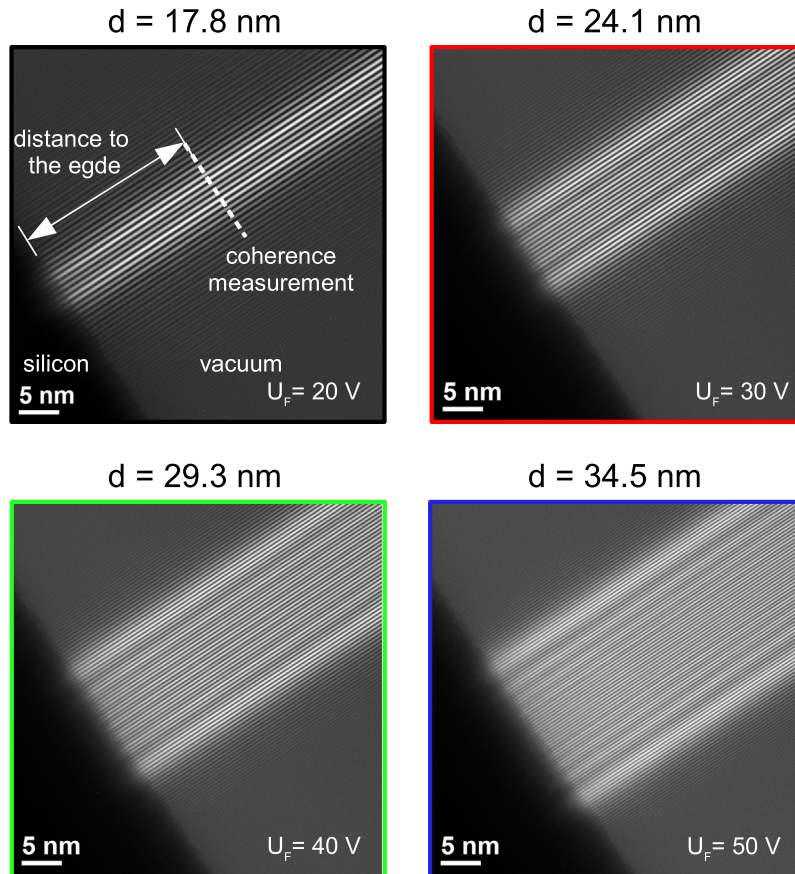


**Fig. 6.** Experimental fringe pattern (acceleration voltage of 200 kV) for different biprism voltages ( $U_F$ ) (colour coded) as a function of distance to a silicon edge. With increasing voltage the shear increases and the fringe spacing decreases. The silicon appears as black shadow in the lower left corner of the images. (For interpretation of the references to colour in this figure legend, the reader is referred to the web version of this paper.)

fringe pattern depicted in Fig. 6. These interference patterns were acquired on a Philips CM200 ST/LL transmission electron microscope. These patterns were evaluated as follows: We fitted tangentially to the surface the hologram intensity (30) and (35) line by line to the experimental data (6), using the Levenberg–Marquardt algorithm with the following free parameters: Degree of coherence  $\mu$ , shear  $d$  and propagation length  $b$ . As fixed parameters we used: Distance between the back focal plane and the biprism plane  $a = 120$  nm, the focal length of the objective lens  $f = 2.9$  mm and the acceleration voltage  $U_A = 200$  kV. For all four fringes pattern we found a physical propagation length of about  $b = 5.43 \pm 0.06$  nm.

The fitted degrees of coherence in dependence on shear  $d$  and distance to the object edge  $y$  are represented in Fig. 7a. Close to the edge, the coherence is dampened due to a strong excitation of surface plasmons. Furthermore, the slope of the coherence decay increases as a function of the shear. This qualitative behaviour is similar to that found for slow aloof beam electrons [44] and shows approximately the same scale invariance ( $\ln \mu \sim -d^2/y^2$ ) as proposed by Machnikowski [58]. Adopted to Machnikowski's model, we therefore fit the function

$$\mu(d, y) = a \exp\left(-\gamma^2 \frac{d^2}{(y - y_0)^2}\right). \quad (38)$$

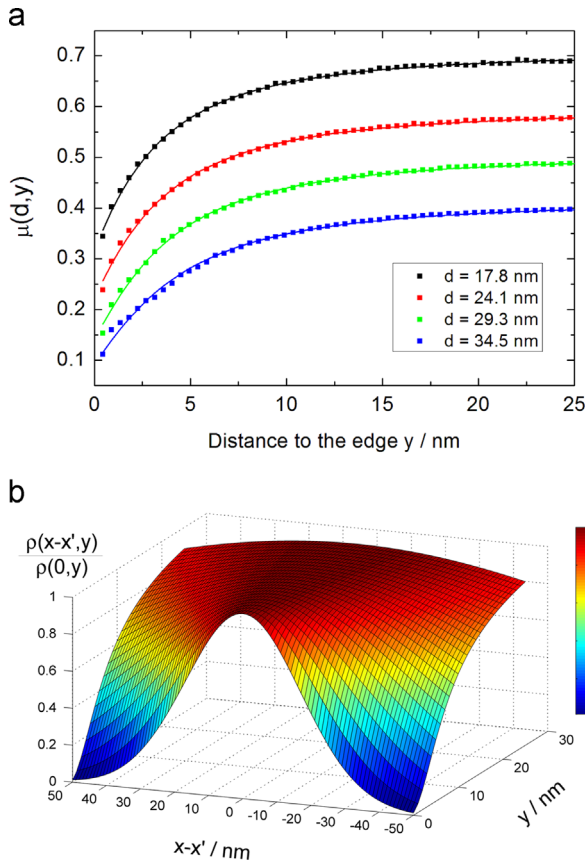


**Fig. 7.** (a) Experimentally determined degree of coherence  $\mu(d, y)$  for different distances to the surface by fitting of (30) with (35) line by line to the intensity profiles at different distances  $y$  to the edge (see white dashed line in Fig. 6). For all of the four fringes pattern we found a propagation length of about  $b = 5.43 \pm 0.06$  nm. To these coherence profiles we fitted a model (38) based on calculations by Machnikowski [58]. (b) Based on this model we obtain the normalized density matrix for the direction parallel to the edge  $(x, x')$  depending on the normal distance to the edge  $y$ . Due to homogeneity in the  $x$ -direction, the density matrix depends only on the difference  $(x - x')$  simplifying its representation here. The absolute density matrix requires further reference measurements to remove artefacts due to inhomogeneous illumination. (For interpretation of the references to colour in this figure legend, the reader is referred to the web version of this paper.)

for the different shears  $d$  to the experimental data represented in Fig. 7a. As free parameters we use  $a$  as amplitude,  $\gamma$  as a factor, which is expected to be constant, and  $y_0$  as effective position of the edge. The fitting results are summarized in Table 1 and depicted in Fig. 7a as solid lines.

The amplitude  $a$  decays systematically with increasing shear as an expected result due to partial coherence of the incoming electron beam (see product in (36)) and transfer properties of the detector (modulation transfer function). These influences can be separated from the state coherence by normalizing the degree of coherence by  $a(d)$ . The result is plotted in Fig. 7b showing the normalized two-dimensional density matrix for the tangential direction  $(x - x')$  depending on the normal distance  $y$ . The parameters  $\gamma$  and  $y_0$  determine the state coherence of the probe electron and are expected to be approximately constant in Ref. [58]. Here, we observe changes, which presumably originate from measurement errors (imperfections of the biprism, charging of the sample) or limits of the model. The position of the effective  $y_0$  edge is shifted to the left (Fig. 7a), because of surface roughness and bending. In the frame of the model, however, we can estimate the angular distribution of scattering parallel to the edge in dependence on the distance  $y$ . Fourier transformation of the ratio  $\mu(d, y)/a(d)$  (38) in the  $x$ -direction yields a Gaussian function with the mean width:

$$\sigma_{\Delta\vartheta}(y) = \frac{\bar{\gamma}}{2\pi|y - y_0|} = \Delta\vartheta(y)k_0. \quad (39)$$

Inserting the mean values of the fitted parameters in Table 1, we obtain a measure for the tangential angular distribution of scattering  $\Delta\vartheta(y)$  in dependence on distance to the edge as

**Table 1**

Fitted parameters corresponding to the model (38) for the four different shears in Fig. 6 and 7a. Amplitude  $a$  decays with increasing shear due to partial coherence of the electron beam (TCC) and modulation transfer function of the detector. The parameters  $\gamma$  and  $y_0$  change slightly around their mean values  $\bar{\gamma} = 0.21 \pm 0.01$  and  $\bar{y}_0 = -5.01 \pm 0.04$  nm.

$d$ (nm)	$a$	$\gamma$	$y_0$ (nm)
17.8	0.71	0.25	-4.98
24.1	0.59	0.21	-5.06
29.3	0.51	0.19	-4.90
34.5	0.41	0.18	-5.10

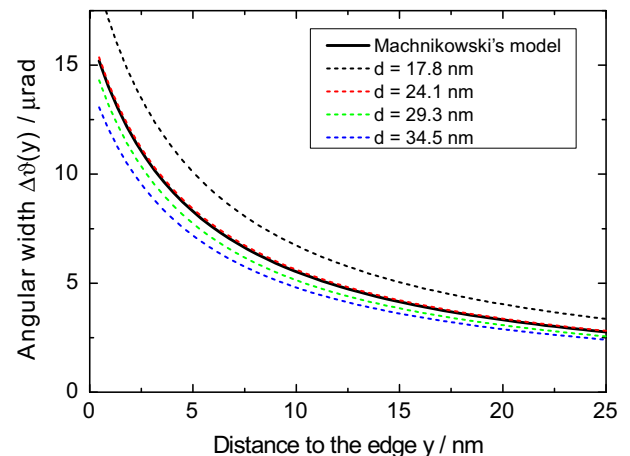


**Fig. 8.** Fitted angular width of scattering  $\Delta\vartheta$  tangential to the surface in dependence on distance to the edge  $y$  (39). For the solid curve we used the mean values for the parameters  $\gamma$  and  $y_0$  represented in Table 1. To demonstrate the precision of the fit to Machnikowski's model we plotted the angular widths based on the individual rows in Table 1 as dashed curves. (For interpretation of the references to colour in this figure legend, the reader is referred to the web version of this paper.)

represented in Fig. 8 (solid curve). Using the errors of these mean values (see caption in Fig. 8), we estimate an relative error of about 20%. The determined angular width of scattering  $\Delta\theta$  shows increased small-angle scattering close to the edge decaying with increasing distance. To demonstrate the precision of a few  $\mu\text{rad}$  of the angular width we additionally plotted the curves for the individual rows in Table 1 (dashed curves in Fig. 8). For a more quantitative comparison with theory a better shear sampling (e.g. by using smaller biprisms) and reference measurements far away from the object are required. Here, the experimental results mainly validate the reconstruction scheme based on the generalized holographic transfer theory.

## 6. Discussion and conclusion

The fringe contrast of the interference pattern carries information related to the off-diagonal elements of the scattered probe electron density matrix and hence the scatterer. This relation is, however, complicated due to the transfer properties of the microscope, preventing a straightforward interpretation. In this work, we presented a scheme for reconstructing the density matrix of the probe electron in a transmission electron microscope using off-axis electron holography based on a generalized concept of the transmission cross-coefficient. We incorporated the formation of interference fringes by the biprism into this transfer theory and defined the holographic transmission cross-coefficient describing the effect of partial coherence on the fringe pattern correctly. We derive conditions allowing to separate the Fresnel diffraction at the biprism from the image plane density matrix. We also show that the image plane density matrix can be related to the object plane density matrix for objects being homogeneous in the normal direction to the biprism. Numerical simulations show that the validity of the approximations is mainly limited at low shears by the diameter of the biprism. For electrons aloofly scattered by planar silicon surfaces we experimentally determine density matrix components parallel to the surface and thus reveal the angular distribution of inelastic scattering in dependence on the distance to the surface. Further experimental improvements like thinner biprisms, reference measurements further away from the object and better shear sampling are required for a quantitative comparisons with theory. The presented method has potential for the analysis of inelastic small-angle scattering in the range of several  $\mu\text{rad}$ , which is conventionally limited by lens aberrations (diffraction lens). Those results might contribute to discussions, e.g. about the quantum-to-classical transitions by small-angle scattering processes.

## Acknowledgements

The authors gratefully acknowledge fruitful, critical and inspiring discussions with Prof. Dr. Hannes Lichte (TU Dresden, Germany). The research leading to these results has received funding from the European Union Seventh Framework Programme under Grant Agreement 312483 - ESTEEM2 (Integrated Infrastructure Initiative - I3).

## Appendix A. Analytic form of the generalized TCC

An analytic expression for the TCC (16) can be found by assuming normalized Gaussian distribution functions for energy  $f_c$  and angular spread  $f_s$  of the electron beam emerging from a finite polychromatic electron source:

$$f_s(\mathbf{k}_\perp) = \frac{1}{\pi \Delta k_x \Delta k_y} e^{-((k_x/\Delta k_x)^2 + (k_y/\Delta k_y)^2)} \quad (\text{A.1})$$

$$f_c(E_c) = \frac{1}{\sqrt{\pi} \Delta E} e^{-(E_c/\Delta E)^2}. \quad (\text{A.2})$$

For the sake of simplicity we neglect the effect of image spread [1,13], which would otherwise require an additional integration over a further probability space. Here, we used the common assumption of incoherent point emitters, which diagonalizes the density matrix at the plane of the source, i.e.  $f_s(\mathbf{k}_\perp, \mathbf{k}'_\perp) = f_s(\mathbf{k}_\perp) \delta(\mathbf{k}_\perp - \mathbf{k}'_\perp)$ . The parameters  $\Delta k_x$  and  $\Delta k_y$  denote components of the vector  $\Delta \mathbf{k}_\perp$  describing the angular spread of the illumination at the object plane. The energy distribution function is parametrized by the energy spread  $\Delta E$ . Inserting (A.1) and (A.2) into (16), the integration over the ensemble variables of the electron beam, i.e.  $(\mathbf{k}_\perp, E_c)$  can be performed analytically after linearizing the phase plate in the usual way:

$$\chi(\mathbf{q} + \mathbf{k}_\perp, E + E_c) \approx \chi(\mathbf{q}, E) + \frac{\pi}{k_0} C_c \frac{E_c}{eU_A} \mathbf{q}^2 + \frac{\partial \chi(\mathbf{q}, E)}{\partial \mathbf{q}} \mathbf{k}_\perp. \quad (\text{A.3})$$

The constant  $C_c$  is the chromatic aberration coefficient and  $U_A$  denotes the acceleration voltage. In this approximation the phase plate is linear and uncorrelated in the ensemble variables  $(\mathbf{k}_\perp, E_c)$ . Thus, we can integrate over the ensemble variable independently. Finally, the integration in (16) yields

$$\text{TCC}(\mathbf{q}, \mathbf{q}', \mathbf{d}, E) \approx E_{sx}(\mathbf{q}, \mathbf{q}', \mathbf{d}, E) E_{sy}(\mathbf{q}, \mathbf{q}', \mathbf{d}, E) E_c(\mathbf{q}, \mathbf{q}', E) \text{WTF}(\mathbf{q}, \mathbf{q}', E). \quad (\text{A.4})$$

The spatial envelope functions  $E_{sx}$  and  $E_{sy}$  describe the transfer of spatial frequencies in the different spatial dimensions due to angular spread and the chromatic envelope function  $E_c$  describes the transfer due to energy spread of the electrons. Note that the chromatic aberration of inelastically scattered electrons arises in (15) by integration over  $E$ . The wave transfer function (WTF) describes the influence of coherent aberrations of the objective lens. For these functions we obtain for  $\mathbf{d} = (d, 0)$ :

$$E_{sx}(\mathbf{q}, \mathbf{q}', d, E) = e^{-(\partial \chi(\mathbf{q}, E)/\partial q_x - \partial \chi(\mathbf{q}', E)/\partial q_x - 2\pi d)^2 (\Delta k_x/2)^2} \quad (\text{A.5})$$

$$E_{sy}(\mathbf{q}, \mathbf{q}', 0, E) = e^{-(\partial \chi(\mathbf{q}, E)/\partial q_y - \partial \chi(\mathbf{q}', E)/\partial q_y)^2 (\Delta k_y/2)^2} \quad (\text{A.6})$$

$$E_c(\mathbf{q}, \mathbf{q}') = e^{-((\pi/2k_0) C_c \Delta E / eU_A)^2 (\mathbf{q}^2 - \mathbf{q}'^2)^2} \quad (\text{A.7})$$

$$\text{WTF}(\mathbf{q}, \mathbf{q}', E) = e^{-i(\chi(\mathbf{q}, E) - \chi(\mathbf{q}', E))}. \quad (\text{A.8})$$

The significant difference to the hitherto theories is that the spatial envelope for the direction perpendicular to the biprism depends on the shear  $d$ . This dependency was already found as anisotropic dampening of the holographic sideband due to the biprism [59,60], but it was not considered as part of a general transfer theory yet.

## Appendix B. Interpretation of centre and sideband

In the following we expand the biprism operator (20) in four terms by

$$B(\mathbf{q}, \mathbf{q}') = \left\{ H_{D_0+} \left( \mathbf{q} + \frac{\mathbf{q}_c}{2} \right) + H_{D_0-} \left( \mathbf{q} - \frac{\mathbf{q}_c}{2} \right) \right\} \times \left\{ H_{D_0+}^* \left( \mathbf{q}' - \frac{\mathbf{q}_c}{2} \right) + H_{D_0-}^* \left( \mathbf{q}' + \frac{\mathbf{q}_c}{2} \right) \right\}. \quad (\text{B.1})$$

The functions  $H_{D_0\pm}$  describe the half space shadowing due to the biprism in Fourier space representation. If the biprism is oriented parallel to the  $y$ -direction, we obtain

$$H_{D_0\pm}(\mathbf{q}) = \frac{1}{2} \left( \delta(q_x) \pm \frac{1}{\pi i q_x} e^{\mp 2\pi i q_x D_0/2} \right) \delta(q_y). \quad (\text{B.2})$$

Here  $q_x$  is the  $\mathbf{q}$  component parallel to the carrier frequency  $\mathbf{q}_c$ . Using the representation (B.1) we can decompose the measured fringe pattern (26) to eventually obtain (30) and (31).



### Appendix C. Special case: elastic off-axis electron holography

In conventional off-axis electron holography, the shear  $\mathbf{d}$  is in most cases much larger than the field of view for the acquired electron hologram. This leads to the effect that the low frequent contributions of the Fresnel fringes are shifted out of the field of view and the high spatial frequent contributions are attenuated by the holographic TCC (27). In this case Fresnel diffraction at the biprism rim does not contribute to the hologram and therefore we can write

$$H_{D_0 \pm}(\mathbf{q}) = \delta(\mathbf{q}). \quad (\text{C.1})$$

Note that this is even better fulfilled in case of double biprism set-ups [61], where no Fresnel fringes occur. This approximation leads to a significant simplification of (31) such that the corresponding density matrices in (30) yield

$$\rho^{\pm \pm} \left( \mathbf{r} \pm \frac{\mathbf{d}}{2}, \mathbf{r} \pm \frac{\mathbf{d}}{2} \right) \approx \rho \left( \mathbf{r} \pm \frac{\mathbf{d}}{2}, \mathbf{r} \pm \frac{\mathbf{d}}{2} \right). \quad (\text{C.2})$$

Here, all contributions for (30) originate now from the same density matrix  $\rho$ . This density matrix is then given by

$$\rho \left( \mathbf{r} \pm \frac{\mathbf{d}}{2}, \mathbf{r} \pm \frac{\mathbf{d}}{2} \right) = \int \rho_s(\mathbf{q}_1, \mathbf{q}'_1, E) \text{TCC} \left( \mathbf{q}_1, \mathbf{q}'_1, \pm \frac{\mathbf{d}}{2}, \pm \frac{\mathbf{d}}{2}, E \right) \times e^{2\pi i(\mathbf{q}_1(\mathbf{r} \pm \mathbf{d}/2) - \mathbf{q}'_1(\mathbf{r} \pm \mathbf{d}/2))} d^2 q_1 d^2 q'_1 dE. \quad (\text{C.3})$$

Again, the dependency of the generalized TCC on the shear underlines the difference of information transfer into centre and sideband. In the special case of pure elastic scattering the density matrix of the probe electron remains in a pure state, i.e. it can be represented as a product of the elastically scattered wave function  $\Psi$  with its complex conjugate:

$$\rho_s(\mathbf{q}_1, \mathbf{q}'_1, E) = \Psi(\mathbf{q}_1) \Psi^*(\mathbf{q}'_1) \delta(E). \quad (\text{C.4})$$

For the off-axis holography set-up, the incoming plane wave passes partially through the object and partially through a field free reference area. Here we consider the biprism orientation into  $y$ -direction and virtually centred at  $x=0$ . The reference area covers the negative half plane  $x < 0$  and the elastically scattered part denoted by  $\Psi_0$  is restricted to the positive half plane  $x \geq 0$ . Consequently we obtain for the total wave at the object exit plane:

$$\Psi(\mathbf{r}) = \begin{cases} \Psi_0(\mathbf{r}) & \text{for } x \geq 0 \\ 1 & \text{for } x < 0. \end{cases} \quad (\text{C.5})$$

Since the shear is assumed to be larger than the field of view, we obtain simplified expressions for both centre bands:

$$\rho \left( \mathbf{r} + \frac{\mathbf{d}}{2}, \mathbf{r} + \frac{\mathbf{d}}{2} \right) = \int \Psi_0(\mathbf{q}_1) \Psi_0^*(\mathbf{q}'_1) \text{TCC}(\mathbf{q}_1, \mathbf{q}'_1, 0, 0) \times e^{2\pi i(\mathbf{q}_1(\mathbf{r} + \mathbf{d}/2) - \mathbf{q}'_1(\mathbf{r} + \mathbf{d}/2))} d^2 q_1 d^2 q'_1 \quad (\text{C.6})$$

$$\rho \left( \mathbf{r} - \frac{\mathbf{d}}{2}, \mathbf{r} - \frac{\mathbf{d}}{2} \right) = \text{TCC}(0, 0, 0, 0) = 1. \quad (\text{C.7})$$

The first term stems from interference of the object wave function  $\Psi_0$  with itself and the second from interference of the reference wave with itself. In the first term we identify the cross-correlation of different scattering vectors weighted by the well-known TCC for conventional high-resolution TEM (19). Interference between reference wave and object wave  $\Psi_0$  determines the sidebands as follows:

$$\rho \left( \mathbf{r} + \frac{\mathbf{d}}{2}, \mathbf{r} - \frac{\mathbf{d}}{2} \right) = \int \Psi_0(\mathbf{q}_1) \text{TCC}(\mathbf{q}_1, 0, \mathbf{d}, 0) e^{2\pi i \mathbf{q}_1(\mathbf{r} + \mathbf{d}/2)} d^2 q_1. \quad (\text{C.8})$$

This expression represents the linear transfer of the object exit wave from the object exit plane into the holographic sideband at the image plane. The phase of the reconstructed image wave is observable in the sense of a phase difference with respect to the

reference wave. Making the usual approximations we find explicit expressions for this TCC in terms of incoherent aberrations described through spatial  $E_s(\mathbf{q}, \mathbf{d})$  and chromatic envelope  $E_c(\mathbf{q})$  functions defining the information limit  $q_{\text{il}}$  of the transmission electron microscope. Scattering information of spatial frequencies with  $|\mathbf{q}| > q_{\text{il}}$  of the object exit wave will not contribute to image information at the image plane due to destructive dephasing as a consequence of variances in energy  $E_c$  and in-plane momentum  $\mathbf{k}_{\perp}$  of the incoming electron beam. Coherent aberrations will then be described by the wave transfer function  $\text{WTF}(\mathbf{q})$  in the known way. For the components of the generalized TCC relevant for the sideband we can then write

$$\text{TCC}(\mathbf{q}, 0, \mathbf{d}, 0) = E_c(\mathbf{q}) E_s(\mathbf{q}, \mathbf{d}) \text{WTF}(\mathbf{q}) \quad (\text{C.9})$$

with the corresponding functions:

$$E_c(\mathbf{q}) = e^{-((\pi/2k_0)C_c \Delta E / eU_A)^2 (\mathbf{q}^2)^2} \quad (\text{C.10})$$

$$E_s(\mathbf{q}, \mathbf{d}) = e^{-((1/2)\partial \chi(\mathbf{q}) / \partial q_x - \pi d)^2 \Delta k_x^2} e^{-((1/2)\partial \chi(\mathbf{q}) / \partial q_y)^2 \Delta k_y^2} \quad (\text{C.11})$$

$$\text{WTF}(\mathbf{q}) = e^{-i\chi(\mathbf{q}, 0)}. \quad (\text{C.12})$$

Here again, we assume the biprism oriented in the  $y$ -direction, hence the shear  $\mathbf{d}$  has a component in the  $x$ -direction only, which will be denoted by  $d$ . The chromatic envelope function  $E_c$  is a radial symmetric function introducing an effective dampening of high spatial frequencies depending on energy width of the electron beam  $\Delta E$  and chromatic aberration coefficient  $C_c$  determined by the electron optical system. Compared to the chromatic envelope, the spatial envelope ( $E_s$ ) exhibits an anisotropy, which is given by the preferential direction of the biprism. This effect was recently found by [59,60]. At spatial frequency  $\mathbf{q} = 0$ , this envelope reduces to

$$E_s(0, \mathbf{d}) = e^{-\pi^2 d^2 \Delta k_x^2}, \quad (\text{C.13})$$

which is equivalent to the degree of coherence for a partial coherent illumination in the far field of the electron source [53,54,26]. This degree of coherence dampens the sideband with respect to the centre band with increasing shear  $d$ . As a consequence the contrast of the holographic fringe pattern will attenuate.

### Appendix D. Separation of Fresnel diffraction and image plane density matrix

The main obstacle for inversion of (31) is the coupling between the holographic TCC and the Fresnel diffraction at the biprism determined by the half-space shadowing functions  $H_{D_0 \pm}$  via  $\mathbf{q}_2$  and  $\mathbf{q}'_2$ . Using the expressions (24), (27) and (B.2) the integration over both variables  $\mathbf{q}_2$  or  $\mathbf{q}'_2$  leads to functions  $D_{\pm}$  (D.1) generally depending on  $\mathbf{q}_1$  or  $\mathbf{q}'_1$  respectively and  $\mathbf{k}_{\perp}$ . For the  $\mathbf{q}_2$  integration we obtain after the variable substitution ( $\mathbf{q}_2 \rightarrow \mathbf{q}_2 + \mathbf{q}_1$ ) the following term depending on  $\mathbf{q}_1$  and  $\mathbf{k}_{\perp}$  in general (for the primed coordinates in analogy):

$$D_{\pm} \left( \mathbf{r} \pm \frac{\mathbf{d}}{2} \right) = \frac{1}{2} \pm \int e^{-2\pi i(b_0/k_0)\mathbf{q}_2 \mathbf{k}_{\perp}} \frac{1}{2\pi i q_{2x}} e^{\mp 2\pi i q_{2x} D_0/2} \delta(q_{2y}) \times e^{-2\pi i(b_0/k_0)\mathbf{q}_2 \mathbf{q}_1} e^{-\pi i(b_0/k_0)\mathbf{q}_2^2} e^{2\pi i \mathbf{q}_2(\mathbf{r} \pm \mathbf{d}/2)} d^2 q_2. \quad (\text{D.1})$$

Since the biprism is orientated in the  $y$ -direction, the integration over the  $y$ -component of  $\mathbf{q}_2$  is trivial. Thus the integration over the  $x$ -component of  $\mathbf{q}_2$  remains and will be denoted by  $q$  in the following. Consequently, the integral (D.1) reduces to

$$D_{\pm} \left( \mathbf{r} \pm \frac{\mathbf{d}}{2} \right) = \frac{1}{2} \pm \int \frac{1}{2\pi i q} e^{-\pi i(b_0/k_0)q^2} e^{2\pi i q \Delta_{\pm}} dq. \quad (\text{D.2})$$



with

$$\Delta_{\pm} = \mp \frac{D_0}{2} + (x \pm \frac{d}{2}) - \frac{b_0}{k_0}(q_{1x} + k_{\perp x}). \quad (\text{D.3})$$

The dependency on the  $y$ -component of  $\mathbf{q}_1$  and  $\mathbf{k}_{\perp}$  cancels, because the biprism has no effect in this direction. The separation of the Fresnel diffraction at the rim of the biprism from the image plane density matrix is now possible, if the  $\mathbf{q}_2$  and  $\mathbf{q}'_2$  integration can be performed independently on  $\mathbf{q}_1$ ,  $\mathbf{q}'_1$  and  $\mathbf{k}_{\perp}$ . We will derive a condition, which approximately removes the dependency of (D.2) on the parameters  $\mathbf{q}_1$  and  $\mathbf{k}_{\perp}$ .

The expression (D.2) can be transformed into the Fresnel integral (F) form by applying the derivative w.r.t.  $\Delta_{\pm}$ , analytical integration w.r.t.  $q$  and subsequent integration w.r.t.  $\Delta_{\pm}$  (D.3) under consideration of the correct boundary conditions. Eventually, we obtain

$$D_{\pm} \left( \mathbf{r} \pm \frac{\mathbf{d}}{2} \right) = F \left( \pm \sqrt{\frac{k_0}{b_0}} \Delta_{\pm} \right) \quad \text{with } F(x) = \frac{1}{\sqrt{i}} \int_{-\infty}^x e^{\pi i \xi^2} d\xi. \quad (\text{D.4})$$

We further consider the function  $D_+$  ( $D_-$  in analogy). After suitable substitution of  $\xi$ , we obtain

$$D_+ \left( \mathbf{r} + \frac{\mathbf{d}}{2} \right) = \frac{1}{\sqrt{i}} \sqrt{\frac{k_0}{b_0}} \int_{-\infty}^{x + d/2 - D_0/2} e^{i\pi(k_0/b_0)(\tilde{x} - (b_0/k_0)(q_{1x} + k_{\perp x}))^2} d\tilde{x}. \quad (\text{D.5})$$

This integral will be evaluated in the frame of stationary phase approximation, which is applicable for small propagation length  $b_0$ . The phase in the integrand becomes stationary, if

$$\tilde{x} = x_0 = \frac{b_0}{k_0}(q_{1x} + k_{\perp x}). \quad (\text{D.6})$$

The integral (D.5) does not depend on this stationary point  $x_0$ , if the upper integration boundary  $(x + d/2 - D_0/2)$  is much larger than the stationary value ( $x_0$ ):

$$x + \frac{d}{2} - \frac{D_0}{2} \gg \frac{b_0}{k_0}(q_{1x} + k_{\perp x}). \quad (\text{D.7})$$

Especially, for the axial part of the fringe pattern ( $|x| \ll (d - D_0)/2$ ), we then obtain the condition:

$$\frac{d}{2} - \frac{D_0}{2} \gg \left| \frac{b_0}{k_0}(q_{1x} + k_{\perp x}) \right|, \quad (\text{D.8})$$

which holds true, if  $d > D_0$ . The absolute value on the right hand side equivalently originates when performing the same analysis for  $D_-$ . In these cases, the integrals do not depend on the stationary point  $x_0$ , hence reduce to

$$\begin{aligned} D_{\pm} \left( \mathbf{r} \pm \frac{\mathbf{d}}{2} \right) &\approx \frac{1}{2} \pm \int \frac{1}{2\pi i q} e^{-\pi i (b_0/k_0) q^2} e^{2\pi i q (\mp D_0/2 + (x \pm d/2))} dq \\ &= F \left( \pm \sqrt{\frac{k_0}{b_0}} \left( \mp \frac{D_0}{2} + \left( x \pm \frac{d}{2} \right) \right) \right). \end{aligned} \quad (\text{D.9})$$

In this approximation, the integration in (31) over  $\mathbf{q}_2$  is independent on the density matrix and the holographic TCC. Then, (31) simplifies to

$$\begin{aligned} \rho^{\pm \pm} \left( \mathbf{r} \pm \frac{\mathbf{d}}{2}, \mathbf{r} \pm \frac{\mathbf{d}}{2}, E \right) &\approx D_{\pm} \left( \mathbf{r} \pm \frac{\mathbf{d}}{2} \right) D_{\pm}^* \left( \mathbf{r} \pm \frac{\mathbf{d}}{2} \right) \\ &\times \int \rho_s(\mathbf{q}_1, \mathbf{q}'_1, E) \text{TCC} \left( \mathbf{q}_1, \mathbf{q}'_1, \pm \frac{\mathbf{d}}{2}, \mp \frac{\mathbf{d}}{2}, E \right) \\ &\times e^{2\pi i (\mathbf{q}_1(\mathbf{r} \pm \mathbf{d}/2) - \mathbf{q}'_1(\mathbf{r} \pm \mathbf{d}/2))} d^2 q_1 d^2 q'_1. \end{aligned} \quad (\text{D.10})$$

The integral in (D.10) describes the influence of the coherent and incoherent aberrations of the TEM onto the state coherence density matrix only.

## Appendix E. Aberrations for a half-plane object

The symmetry of the object (Fig. 5) implies diagonality in Fourier space in the direction of the  $x$ -components of the electron's wave vector  $\mathbf{q}$ . Consequently, the following components of the TCC contribute to the integral in (D.10):

$$\text{TCC} \left( \begin{pmatrix} q_x \\ q_y \end{pmatrix}, \begin{pmatrix} q_x \\ q_y \end{pmatrix}, \pm \frac{\mathbf{d}}{2}, \mp \frac{\mathbf{d}}{2}, E \right). \quad (\text{E.1})$$

A cross-talk between  $q_x$  (parallel to the surface) and  $q_y$  (perpendicular) appears due to higher order aberrations prohibiting a separation of the two dimensions. Considering that the dominating first and third order coherent aberrations in the TCC determining the phase difference depend on

$$\begin{aligned} \chi \left( \begin{pmatrix} q_x \\ q_y \end{pmatrix}, E \right) - \chi \left( \begin{pmatrix} q_x \\ q'_y \end{pmatrix}, E \right) &\approx \frac{\pi D_z}{k_0} (q_y^2 - q_y'^2) \\ &+ \frac{\pi C_s}{2k_0^3} (q_y^4 - q_y'^4 + 2q_x^2 (q_y^2 - q_y'^2)). \end{aligned} \quad (\text{E.2})$$

While in the first order aberrations (e.g. defocus  $D_z$ ) the  $q_x$  dependency vanishes, the third order aberrations (e.g. spherical aberration  $C_s$ ) induce a coupling between the  $q_x$  and  $q_y$ . This coupling is negligible, if  $q_y^2 + q_y'^2 \gg 2q_x^2$  holds true. Since this phase shift becomes relevant for wave vector components much larger than the characteristic wave vector due to energy transfer, the inequality is fulfilled for all relevant wave vectors. Due to vanishing coupling in first order, the chromatic aberration only affects the normal direction of the surface. However, the spatial envelope functions again incorporate couplings. The dampening in the normal direction to the surface decouples from the  $x$ -direction, if  $q_y^2, q_y'^2 \gg q_x^2$ . The dampening parallel to the surface is dominated by the illumination aperture only according to (C.13), if

$$q_y^2 - q_y'^2 \ll \frac{dk_0^3}{C_s q_x} \quad (\text{E.3})$$

holds true. This is fulfilled for 200 keV electrons, a spherical aberration in the order of  $C_s = 1$  mm, a shear in the order of 10 nm and an energy transfer around 10 eV ( $q_x \approx q_E$ ).

## References

- [1] M. Haider, P. Hartel, H. Müller, S. Uhlemann, J. Zach, Information transfer in a TEM corrected for spherical and chromatic aberration, *Microsc. Microanal.* 16 (2010) 393–408.
- [2] J. Frank, The envelope of electron microscopy transfer functions for partially coherent illumination, *Optik* 38 (1973) 519–536.
- [3] F.J. García de Abajo, Optical excitations in electron microscopy, *Rev. Mod. Phys.* 82 (2010) 209–275.
- [4] A. Howie, Inelastic scattering of electrons by crystals: I. The theory of small-angle inelastic scattering, *Proc. R. Soc. Lond. A* 271 (1963) 268–287.
- [5] L. Reimer, R. Rennekamp, Imaging and recording of multiple scattering effects by angular resolved electron energy loss spectroscopy, *Ultramicroscopy* 28 (1989) 258–265.
- [6] Y.Y. Wang, S.C. Cheng, V.P. Dravid, F.C. Zhang, Momentum-transfer resolved electron energy loss spectroscopy of solids: problems, solutions and applications, *Ultramicroscopy* 59 (1995) 109–119.
- [7] L. Gu, V. Srot, W. Sigle, C. Koch, P. van Aken, F. Scholz, S.B. Thapa, C. Kirchner, M. Jetter, M. Rühle, Band-gap measurements of direct and indirect semiconductors using monochromated electrons, *Phys. Rev. B* 75 (2007) 195214.
- [8] H. Kohl, H. Rose, Theory of image formation by inelastically scattered electrons in the electron microscope, *Adv. Electron. Electron Phys.* 65 (1985) 173–227.
- [9] S.L. Dudarev, L.-M. Peng, M.J. Whelan, Correlations in space and time and dynamical diffraction of high-energy electrons by crystals, *Phys. Rev. B* 48 (1993) 13408.

- [10] A. Rother (Lubk), T. Gemming, H. Lichte, The statistics of the thermal motion of the atoms during imaging process in transmission electron microscopy and related techniques, *Ultramicroscopy* 109 (2009) 139–146.
- [11] F.J. García de Abajo, Optical emission from the interaction of fast electrons with metallic films containing a circular aperture: a study of radiative decoherence of fast electrons, *Phys. Rev. Lett.* 102 (2009) 237401.
- [12] A. Howie, Mechanisms of decoherence in electron microscopy, *Ultramicroscopy* 111 (2011) 761–767.
- [13] S. Uhlemann, H. Müller, P. Hartel, J. Zach, M. Haider, Thermal magnetic field noise limits resolution in transmission electron microscopy, *Phys. Rev. Lett.* 111 (2013) 046101.
- [14] L. van Hove, Correlations in space and time and born approximation scattering in systems of interacting particles, *Phys. Rev.* 95 (1954) 249–262.
- [15] H. Rose, Image formation by inelastically scattered electrons in electron microscopy, *Optik* 45 (1976) 139–158.
- [16] H. Rose, Information transfer in transmission electron microscopy, *Ultramicroscopy* 15 (1984) 173–192.
- [17] M. Born, E. Wolf, *Principles of Optics, Electromagnetic Theory of Propagation, Interference and Diffraction of Light*, sixth (corrected) edition, Pergamon Press, 1991, ISBN 0-08-026482-4.
- [18] L. Mandel, E. Wolf, Coherence properties of optical fields, *Rev. Mod. Phys.* 37 (1965) 231–287.
- [19] J.v. Neumann, *Thermodynamik quantenmechanischer Gesamtheiten*, Gött. Nachr. 3 (1927) 273–291.
- [20] D. ter Haar, Theory and applications of the density matrix, *Rep. Prog. Phys.* 24 (1961) 304–362.
- [21] H. Kohl, Image formation by inelastically scattered electrons: image of a surface plasmon, *Ultramicroscopy* 11 (1983) 53–66.
- [22] J. Verbeeck, D. van Dyck, H. Lichte, P. Potapov, P. Schattschneider, *Ultramicroscopy* 102 (2005) 239–255.
- [23] P. Schattschneider, H. Lichte, Correlation and the density-matrix approach to inelastic electron holography in solid state plasmas, *Phys. Rev. B* 71 (2005) 045130.
- [24] Z. Lee, H. Rose, R. Hambach, P. Wachsmuth, U. Kaiser, The influence of inelastic scattering on EFTEM images exemplified at 20 kV for graphene and silicon, *Ultramicroscopy* 134 (2013) 102–112.
- [25] C. Dinges, A. Berger, H. Rose, Simulation of TEM images considering phonon and electronic excitations, *Ultramicroscopy* 60 (1995) 49–70.
- [26] H. Müller, H. Rose, P. Schorsch, A coherence function approach to image simulation, *J. Microsc.* 190 (1998) 73–88.
- [27] P. Schattschneider, M. Nelhiebel, B. Jouffrey, Density matrix of inelastically scattered fast electrons, *Phys. Rev. B* 59 (1999) 10959.
- [28] P. Schattschneider, M. Nelhiebel, H. Souchay, B. Jouffrey, The physical significance of the mixed dynamic form factor, *Micron* 31 (2000) 333.
- [29] P. Schattschneider, S. Rubino, C. Hébert, J. Ruzs, J. Kuneš, P. Novák, E. Carlino, M. Fabrizio, G. Panaccione, G. Rossi, Detection of magnetic circular dichroism using a transmission electron microscope, *Nature* 441 (2006) 486–488.
- [30] J. Verbeeck, P. Schattschneider, A. Rosenauer, Image simulation of high resolution energy filtered TEM images, *Ultramicroscopy* 109 (2009) 350–360.
- [31] W.H. Zurek, *Rev. Mod. Phys.* 75 (2003) 715–775.
- [32] M. Schlosshauer, Decoherence, the measurement problem, and interpretations of quantum mechanics, *Rev. Mod. Phys.* 76 (2004) 1267–1305.
- [33] D. Gabor, A new microscopic principle, *Nature* 161 (1948) 777–778.
- [34] J.M. Cowley, Twenty forms of electron holography, *Ultramicroscopy* 41 (1992) 335–348.
- [35] H. Lichte, M. Lehmann, Electron holography—basics and applications, *Rep. Prog. Phys.* 71 (2008) 016102.
- [36] G. Möllenstedt, H. Düker, Beobachtungen und Messungen an Biprisma-Interferenzen mit Elektronenwellen, *Z. Phys.* 145 (1956) 377–397.
- [37] M.R. McCartney, D.J. Smith, Electron holography: phase imaging with nanometer resolution, *Annu. Rev. Mater. Res.* 37 (2007) 729.
- [38] P.A. Midgley, R.E. Dunin-Borkowski, Electron tomography and holography in materials science, *Nat. Mater.* 8 (2009) 271–280.
- [39] H. Lichte, F. Börrnert, A. Lenk, A. Lubk, F. Röder, J. Sickmann, S. Sturm, K. Vogel, D. Wolf, Electron holography for fields in solids: problems and progress, *Ultramicroscopy* 134 (2013) 126–134.
- [40] A. Harscher, H. Lichte, J. Mayer, Interference experiments with energy filtered electrons, *Ultramicroscopy* 69 (1997) 201–209.
- [41] H. Lichte, B. Freitag, Inelastic electron holography, *Ultramicroscopy* 81 (2000) 177–186.
- [42] P.L. Potapov, H. Lichte, J. Verbeeck, D. van Dyck, Experiments on inelastic electron holography, *Ultramicroscopy* 106 (2006) 1012–1018.
- [43] P.L. Potapov, J. Verbeeck, P. Schattschneider, H. Lichte, D. van Dyck, Inelastic electron holography as a variant of the Feynman thought experiment, *Ultramicroscopy* 107 (2007) 559–567.
- [44] P. Sonnentag, F. Hasselbach, Measurement of decoherence of electron waves and visualization of the quantum-classical transition, *Phys. Rev. Lett.* 98 (2007) 200402.
- [45] J. Verbeeck, G. Bertoni, P. Schattschneider, *Ultramicroscopy* 108 (2008) 263–269.
- [46] R.H. Wade, J. Frank, Electron microscope transfer functions for partially coherent axial illumination and chromatic defocus spread, *Optik* 49 (1977) 81–92.
- [47] R.H. Wade, W.K. Jenkins, Tilted beam electron microscopy: the effective coherent aperture, *Optik* 50 (1979) 1–17.
- [48] K. Ishizuka, Contrast transfer of crystal images in TEM, *Ultramicroscopy* 5 (1980) 55–65.
- [49] C.T. Koch, A flux-preserving non-linear inline holography reconstruction algorithm for partially coherent electrons, *Ultramicroscopy* 108 (2008) 141–150.
- [50] C.T. Koch, A. Lubk, Off-axis and inline electron holography: a quantitative comparison, *Ultramicroscopy* 110 (2010) 460–471.
- [51] J.R. Anglin, J.P. Paz, W.H. Zurek, Deconstructing decoherence, *Phys. Rev. A* 55 (1997) 4041–4053.
- [52] A. Howie, Surface reactions and excitations, *Ultramicroscopy* 11 (1983) 141–148.
- [53] P.H. van Cittert, Die wahrscheinliche Schwingungs-verteilung in einer von einer Lichtquelle direkt oder mittels einer Linse beleuchteten Ebene, *Physica* 1 (1934) 201–210.
- [54] F. Zernike, The concept of degree of coherence and its application to optical problems, *Physica* 5 (1938) 785–795.
- [55] H. Lichte, Performance limits of electron holography, *Ultramicroscopy* 108 (2008) 256–262.
- [56] F. Houdellier, M.J. Hytch, Diffracted phase and amplitude measurements by energy-filtered convergent-beam holography (CHEF), *Ultramicroscopy* 108 (2008) 285–294.
- [57] P. Schattschneider, J. Verbeeck, *Ultramicroscopy* 108 (2008) 407–414.
- [58] P. Machnikowski, Theory of which path dephasing in single electron interference due to trace in conductive environment, *Phys. Rev. B* 73 (2006) 155109.
- [59] W. Koch, A. Lubk, F. Grossmann, H. Lichte, R. Schmidt, Coherent and incoherent effects on the imaging an scattering process in transmission electron microscopy and off-axis electron holography, *Ultramicroscopy* 110 (2010) 1397–1403.
- [60] M. Linck, Off-axis Holographie im aberrationskorrigierten Transmissionselektronenmikroskop, (Ph.D. thesis), TU Dresden, 2010.
- [61] K. Harada, A. Tonomura, Y. Togawa, T. Akashi, T. Matsuda, Double-biprism electron interferometry, *Appl. Phys. Lett.* 84 (2004) 3229–3231.